The Astrophysical Journal, 686:749–778, 2008 October 20

IMPROVED COSMOLOGICAL CONSTRAINTS FROM NEW, OLD, AND COMBINED SUPERNOVA DATA SETS

M. Kowalski,[1] D. Rubin,[2,3] G. Aldering,[2] R. J. Agostinho,[4] A. Amadon,[5] R. Amanullah,[6] C. Balland,[7] K. Barbary,[2,3] G. Blanc,[8] P. J. Challis,[9] A. Conley,[10] N. V. Connolly,[11] R. Covarrubias,[12] K. S. Dawson,[2] S. E. Deustua,[13] R. Ellis,[14] S. Fabbro,[15] V. Fadeyev,[16] X. Fan,[17] B. Farris,[18] G. Folatelli,[12] B. L. Frye,[19] G. Garavini,[20] E. L. Gates,[21] L. Germany,[22] G. Goldhaber,[2,3] B. Goldman,[23] A. Goobar,[20] D. E. Groom,[2] J. Haissinski,[24] D. Hardin,[7] I. Hook,[25] S. Kent,[26] A. G. Kim,[2] R. A. Knop,[27] C. Lidman,[28] E. V. Linder,[6] J. Mendez,[29,30] J. Meyers,[2,3] G. J. Miller,[31] M. Moniez,[24] A. M. Mourão,[15] H. Newberg,[32] S. Nobili,[20] P. E. Nugent,[2] R. Pain,[7] O. Perdereau,[24] S. Perlmutter,[2,3] M. M. Phillips,[33] V. Prasad,[2] R. Quimby,[14] N. Regnault,[7] J. Rich,[5] E. P. Rubenstein,[34] P. Ruiz-Lapuente,[30] F. D. Santos,[35] B. E. Schaefer,[36] R. A. Schommer,[37] R. C. Smith,[38] A. M. Soderberg,[14] A. L. Spadafora,[2] L.-G. Strolger,[39] M. Strovink,[2,3] N. B. Suntzeff,[40] N. Suzuki,[2] R. C. Thomas,[2] N. A. Walton,[41] L. Wang,[40] W. M. Wood-Vasey,[9] and J. L. Yun[4] (The Supernova Cosmology Project)

Received 2007 October 25; accepted 2008 April 2

ABSTRACT

We present a new compilation of Type Ia supernovae (SNe Ia), a new data set of low-redshift nearby-Hubble-flow SNe, and new analysis procedures to work with these heterogeneous compilations. This "Union" compilation of 414 SNe Ia, which reduces to 307 SNe after selection cuts, includes the recent large samples of SNe Ia from the Supernova Legacy Survey and ESSENCE Survey, the older data sets, as well as the recently extended data set of distant supernovae observed with the *Hubble Space Telescope* (*HST*). A single, consistent, and blind analysis procedure is used for all the various SN Ia subsamples, and a new procedure is implemented that consistently weights the heterogeneous data sets and rejects outliers. We present the latest results from this Union compilation and discuss the cosmological constraints from this new compilation and its combination with other cosmological measurements (CMB and BAO). The constraint we obtain from supernovae on the dark energy density is $\Omega_\Lambda = 0.713^{+0.027}_{-0.029}(\mathrm{stat})^{+0.036}_{-0.039}(\mathrm{sys})$, for a flat, ΛCDM universe. Assuming a constant equation of state parameter, w, the combined constraints from SNe, BAO, and

[1] Institut für Physik, Humboldt-Universität zu Berlin, Newtonstrasse 15, Berlin 12489, Germany.
[2] E. O. Lawrence Berkeley National Laboratory, 1 Cyclotron Road, Berkeley, CA 94720.
[3] Department of Physics, University of California Berkeley, Berkeley, CA 94720-7300.
[4] Centro de Astronomia e Astrofísica da Universidade de Lisboa, Observatório Astronómico de Lisboa, Tapada da Ajuda, 1349-018 Lisbon, Portugal.
[5] DSM/DAPNIA, CEA/Saclay, 91191 Gif-sur-Yvette Cedex, France.
[6] Space Sciences Laboratory, University of California Berkeley, Berkeley, CA 94720.
[7] LPNHE, CNRS-IN2P3, University of Paris VI & VII, Paris, France.
[8] APC, Université Paris 7, 10 rue Alice Domon et Léonie Duquet, 75205 Paris Cedex 13, France.
[9] Center for Astrophysics, Harvard University, 60 Garden Street, Cambridge, MA 02138.
[10] Department of Astronomy and Astrophysics, University of Toronto, 60 St. George Street, Toronto, ON M5S 3H8, Canada.
[11] Department of Physics, Hamilton College, Clinton, NY 13323.
[12] Observatories of the Carnegie Institution of Washington, 813 Santa Barbara Street, Pasadena, CA 9110.
[13] American Astronomical Society, 2000 Florida Avenue, NW, Suite 400, Washington, DC 20009.
[14] California Institute of Technology, East California Boulevard, Pasadena, CA 91125.
[15] CENTRA e Dep. de Fisica, IST, Avenida Rovisco Pais, 1049 Lisbon, Portugal.
[16] Department of Physics, University of California Santa Cruz, Santa Cruz, CA 95064.
[17] Steward Observatory, University of Arizona, Tucson, AZ 85721.
[18] Department of Physics, University of Illinois at Urbana-Champaign, 1110 West Green, Urbana, IL 61801-3080.
[19] Department of Physical Sciences, Dublin City University, Glasnevin, Dublin 9, Ireland.
[20] Department of Physics, Stockholm University, Albanova University Center, S-106 91 Stockholm, Sweden.
[21] Lick Observatory, P.O. Box 85, Mount Hamilton, CA 95140.
[22] Centre for Astrophysics and Supercomputing, Swinburne University of Technology, John Street, Hawthorn, VIC 3122, Australia.
[23] M.P.I.A., Königstuhl 17, 69117 Heidelberg, Germany.
[24] Laboratoire de l'Accélerateur Linéaire, IN2P3-CNRS, Université Paris Sud, B.P. 34, 91898 Orsay Cedex, France.
[25] Sub-Department of Astrophysics, University of Oxford, Denys Wilkinson Building, Keble Road, Oxford OX1 3RH, UK.
[26] Fermi National Accelerator Laboratory, P.O. Box 500, Batavia, IL 60510.
[27] Department of Physics and Astronomy, Vanderbilt University, Nashville, TN 37240.
[28] European Southern Observatory, Alonso de Cordova 3107, Vitacura, Casilla 19001, Santiago 19, Chile.
[29] Isaac Newton Group, Apartado de Correos 321, 38780 Santa Cruz de La Palma, Islas Canarias, Spain.
[30] Department of Astronomy, University of Barcelona, Barcelona, Spain.
[31] Southwestern College, Department of Astronomy, 900 Otay Lakes Road, Chula Vista, CA 91910.
[32] Physics Department, Rensselaer Polytechnic Institute, SC1C25, Troy, NY 12180.
[33] Las Campanas Observatory, Carnegie Observatories, Casilla 601, La Serena, Chile.
[34] Advanced Fuel Research, Inc., 87 Church Street, East Hartford, CT 06108.
[35] Department of Physics, Faculty of Sciences, University of Lisbon, Ed. C8, Campo Grande, 1749-016 Lisbon, Portugal.
[36] Louisiana State University, Department of Physics and Astronomy, Baton Rouge, LA 70803.
[37] Deceased.
[38] Cerro Tololo Inter-American Observatory, Casilla 603, La Serena, Chile.
[39] Department of Physics and Astronomy, Western Kentucky University, Bowling Green, KY.
[40] Department of Physics, Texas A&M University, College Station, TX 77843.
[41] Institute of Astronomy, Madingley Road, Cambridge CB3 0HA, UK.

CMB give $w = -0.969^{+0.059}_{-0.063}(\mathrm{stat})^{+0.063}_{-0.066}(\mathrm{sys})$. While our results are consistent with a cosmological constant, we obtain only relatively weak constraints on a w that varies with redshift. In particular, the current SN data do not yet significantly constrain w at $z > 1$. With the addition of our new nearby Hubble-flow SNe Ia, these resulting cosmological constraints are currently the tightest available.

Subject headings: cosmological parameters — cosmology: observations — supernovae: general

Online material: color figures, machine-readable tables

1. INTRODUCTION

The evidence for dark energy has evolved from the first hints, for the case of a flat universe (Perlmutter et al. 1998; Garnavich et al. 1998; Schmidt et al. 1998), through the more definite evidence for the general case of unconstrained curvature (Riess et al. 1998; Perlmutter et al. 1999), to the current work, which aims to explore the properties of dark energy (for a review, see Perlmutter & Schmidt 2003). Several new cosmological measurement techniques and several new Type Ia supernova (SN Ia) data sets have helped begin the laborious process of narrowing in on the parameters that describe the cosmological model. The SN Ia measurements remain a key ingredient in all current determinations of cosmological parameters (see, e.g., the recent CMB results [Dunkley et al. 2008]). It is therefore necessary to understand how the current world data set of SN Ia measurements is constructed and how it can be used coherently, particularly since no one SN Ia sample by itself provides an accurate cosmological measurement.

Until recently, the SN Ia compilations (e.g., Riess et al. 1998; Perlmutter et al. 1999; Tonry et al. 2003; Knop et al. 2003; Astier et al. 2006; Wood-Vasey et al. 2007) primarily consisted of a relatively uniform high-redshift ($z \sim 0.5$) data set from a single study put together with a low-redshift ($z \sim 0.05$) sample collected in a different study or studies. However, once there were several independent data sets at high redshift, it became more important and interesting to see the cosmological constraints obtainable by combining several groups' work. Riess et al. (2004, 2007) provided a first compilation analysis of this kind, drawing on data chosen from Perlmutter et al. (1999), Riess et al. (1998), Schmidt et al. (1998), Knop et al. (2003), Tonry et al. (2003), and Barris et al. (2004). Many of the subsequent cosmology studies have used this compilation as the representation of the SN Ia sample, in particular the selection of supernovae that Riess et al. (2004, 2007) nicknamed the "Gold" sample. Other recent compilations that have been used are those of Wood-Vasey et al. (2007) and Davis et al. (2007).

At present a number of updates should be made to the SN Ia data sets, and a number of analysis issues should be addressed, including several that will recur with every future generation of SN compilations. These include the following major goals:

1. It is important to add a new low-redshift SN Ia sample to complement the large and rapidly growing number of distant SNe. Especially valuable are the SNe in the smooth, nearby Hubble flow (z above $\sim$0.02). Since this part of the Hubble diagram is currently not well constrained, new nearby SNe lead to a relatively large incremental improvement (Linder 2006). It is interesting to note that the largest contribution in this redshift range still comes from the landmark Calan/Tololo survey (Hamuy et al. 1996).
2. The analysis should reflect the heterogeneous nature of the data set. In particular, it is important that a sample of poorer quality will not degrade the impact of the higher quality data, such as the Supernova Legacy Survey (SNLS) and ESSENCE high-redshift data sets, which have recently been published.
3. The different supernova data sets should be analyzed with the same analysis procedure. The previous compilations combined measurements and peak-magnitude fits that were obtained with disparate light curve fitting functions and analysis procedures, particularly for handling the color correction for both extinction and any intrinsic color-luminosity relation.
4. A reproducible, well-characterized approach to selecting the good SNe Ia and rejecting the questionable and outlier SNe should be used. Previous compilations relied to a large extent on the heterogeneous classification information provided by the original authors. The selection process was somewhat subjective: The Gold compilation of Riess et al. (2004, 2007) excluded SNe that Knop et al. (2003) considered comparably well-confirmed SNe Ia.
5. To the extent possible, the analysis should not introduce biases into the fit, including some that have only recently been recognized as being present in methods of determining extinction properties of SNe Ia.

To reach the goal of carrying out these improvements, we present in this paper a new SN compilation, a new nearby-Hubble-flow SN Ia data set, and new analysis procedures. Several additional smaller enhancements are also presented.

With respect to goal 1, it is important to note that both nearby and distant supernovae are needed to measure cosmological parameters. The brightness of nearby supernovae in the Hubble flow is compared to that of high-redshift supernovae, which—following the dynamics of the universe—might appear dimmer or brighter than expected for a reference cosmology. Nearby SN light curves typically have better observational coverage and signal-to-noise ratio (S/N) than their high-redshift counterparts. However, they are significantly more difficult to discover since vast amounts of sky have to be searched to obtain a sizable number of supernovae, due to the small volume of the low-redshift universe. We present light curves from the Supernova Cosmology Project (SCP) Spring 1999 Nearby Supernova Campaign (Aldering 2000), which consisted primarily of wide-field magnitude-limited searches and extensive photometric and spectroscopic follow-up observations using a large number of ground-based telescopes. We provide *BVRI* light curves for eight nearby supernovae in the Hubble flow.

We then address goal 2 by combining the new data sample with published data of nearby and distant supernovae to construct the largest Hubble diagram to date (but presumably not for long). In this combination we adjust the weight of SNe belonging to a sample to reflect the dispersion we determine for the sample. With our prescription, SN samples with significant unaccounted-for statistical or systematic uncertainties are effectively deweighted.

All SN light curves are fitted consistently in the observer frame system using the spectral-template–based fit method of Guy et al. (2005) (also known as SALT). Where possible, the original bandpass functions are used (goal 3).

To address goal 4, we adopt a robust analysis technique based on outlier rejection that we show is resilient against contamination. The analysis strategy was developed to limit the influence of human subjectivity. Spectroscopic classification is arguably the most subjective component of SN cosmology (primarily because

of the observational challenges associated with high-redshift supernova spectroscopy), and we avoid decisions of whether to include a specific SN that are based on spectroscopic features that go beyond that of the authors' classification.

Following Conley et al. (2006), the full analysis chain was developed in a blind fashion—that is, hiding the best-fitting cosmological parameters until the analysis was finalized. This helps resist the impulse to stop searching for systematic effects once the "right" answer is obtained. We derive constraints on the cosmological parameters, taking care to test and remove possible sources of bias introduced in the fitting procedure (goal 5).

The paper is organized as follows. In § 2 we methodically present the data reduction and photometric calibration of the light curves from the SCP Nearby 1999 Supernova Campaign: the reader more interested in goals 2–5 and the subsequent cosmological analysis might want to only skim this section. In § 3 we combine the new supernovae with a large set of nearby and high-redshift supernovae from the literature and fit the full set of light curves in a consistent manner. We then proceed to determine stringent constraints on the dynamics of the universe. Section 4 explains the methods employed for cosmological parameter estimation, which includes blinding the analysis and using robust statistics. We evaluate the systematic errors of the measurements in § 5 and summarize the resulting constraints on Ω_M, Ω_Λ, w, and other parameters in § 6.

2. A NEW SAMPLE OF NEARBY SUPERNOVAE

The SN light curve data presented in this paper were obtained as part of the SCP Nearby 1999 Supernova Campaign (Aldering 2000). The search portion of this campaign was designed to discover Type Ia supernovae in the smooth nearby Hubble flow and was performed in collaboration with a number of wide-field CCD imaging teams: EROS-II (Blanc et al. 2004), NGSS (Strolger 2003), QUEST-I (Rengstorf et al. 2004), NEAT (Pravdo et al. 1999), and Spacewatch (Nugent et al. 1999b). In some cases the wide-field searches were focused entirely on supernova discovery (EROS-II and NGSS), while in other cases the primary data had different scientific goals, such as discovery of near-Earth objects (NEAT, Spacewatch), quasars, or microlenses (QUEST-I). The wide-field cameras operated in either point and track (NGSS, NEAT, EROS-II) or driftscan (QUEST-I, Spacewatch) modes, and in total covered hundreds of square degrees per night. Over a 2 month period beginning in 1999 February, a total of more than 1300 deg^2 was monitored for SNe. Since the search was magnitude limited—no specific galaxies were targeted—it resembles typical searches for high-redshift supernovae. This is important because common systematics effects, such as Malmquist bias, are then expected to more nearly cancel when comparing low-redshift with high-redshift supernovae.

A total of 32 spectroscopically confirmed SNe were discovered by the search component of this campaign. Of these, 22 were of Type Ia, and 14 (of these) were discovered near maximum light, making them useful for cosmological studies. In addition, early alerts of potential SNe by LOTOSS (Filippenko et al. 2001) and similar galaxy-targeted searches, and the WOOTS-I (Gal-Yam et al. 2008) and MSACS (Germany et al. 2004) cluster-targeted searches, provided a supplement to the primary sample as the wide-area searches ramped up. Extensive spectroscopic screening and follow-up was obtained using guest observer time on the CTIO 4 m, KPNO 4 m, APO 3.5 m, Lick 3 m, NOT, INT, MDM 2.4 m, ESO 3.6 m, and WHT 4.2 m telescopes. The results of these observations have been reported elsewhere (Kim et al. 1999a 1999b; Aldering et al. 1999; Strolger et al. 1999a, 1999b, 2002; Gal-Yam et al. 1999; Nugent et al. 1999a, 1999c; Blanc et al. 2004; Garavini et al. 2004, 2005, 2007; Folatelli 2004). Photometric follow-up observations were obtained with the LICK 1 m, YALO 1 m, CTIO 0.9 m, CTIO 1.5 m, MARLY, Danish 1.5 m, ESO 3.6 m, KPNO 2.1 m, JKT 1 m, CFHT 3.6 m, KECK-I 10 m, WIYN 3.5 m, and MLO 1 m telescopes. These consist of *UBVRI* photometry with a nominal cadence of 3–7 days. The follow-up observations were performed between February and 1999 June, and additional reference images to determine the contribution of host galaxy light contamination were obtained in spring 2000.

TABLE 1
Summary of Supernova Coordinates and Redshifts

Name	R.A. (J2000.0)	Decl. (J2000.0)	Redshift	IAUC
SN1999aa.....	08 27 42.03	+21 29 14.8	0.0142	7180,7109
SN1999ao.....	06 27 26.37	−35 50 24.2	0.0539	7124
SN1999aw.....	11 01 36.37	−06 06 31.6	0.038	7130
SN1999ar	09 20 16.00	+00 33 39.6	0.1548	7125
SN1999bi	11 01 15.76	−11 45 15.2	0.1227	7136
SN1999bm	12 45 00.84	−06 27 30.2	0.1428	7136
SN1999bn	11 57 00.40	−11 26 38.4	0.1285	7136
SN1999bp	11 39 46.42	−08 51 34.8	0.0770	7136

Notes.—Units of right ascension are hours, minutes, and seconds, and units of declination are degrees, arcminutes, and arcseconds. The heliocentric redshift was determined using narrow host-galaxy features for all but one SN. In the case of SN 1999aw: due to the faintness of its host, the redshift was determined from the SN spectra.

From this campaign we present *BVRI* light curves for the eight Type Ia SNe that fall into the redshift range $0.015 \lesssim z \lesssim 0.15$ and for which we were able to obtain enough photometric follow-up data: SN 1999aa (Armstrong & Schwartz 1999; Qiao et al. 1999), SN 1999ao (Reiss et al. 1999), SN 1999ar (Strolger et al. 1999b), SN 1999aw (Gal-Yam et al. 1999), and SN 1999bi, SN 1999bm, SN 1999bn, and SN 1999bp (Kim et al. 1999a). Further information on these SNe is summarized in Table 1. Photometric data on SN 1999aw have already been published by Strolger et al. (2002); here we present a self-consistent reanalysis of that photometry.

2.1. *Data Reduction and Photometric Calibration*

The data were preprocessed using standard algorithms for bias and flat field correction. In addition, images that showed significant fringing were corrected by subtracting the structured sky residuals obtained from the median of fringing-affected images. Reflecting an original goal of this program—to obtain data for nearby SNe Ia matching that of the high-redshift data of Perlmutter et al. (1999)—we have employed aperture photometry to measure the SN light curves. For measurement of moderately bright point sources projected onto complex host galaxy backgrounds in fields sparsely covered by foreground stars, aperture photometry has higher systematic accuracy, but slightly lower statistical precision, than PSF fitting. We used an aperture radius equal to the FWHM of a point source, as determined from the field stars in the image. The aperture correction, which is defined as the fraction of total light that is outside the FWHM radius, is determined by approximating an infinite aperture by a $4 \times$ FWHM radius aperture. The aperture correction for a given image is then obtained by a weighted average for all the stars in the field.

In all, photometric observations employed a total of 12 different telescopes and 14 different detector/filter systems. This presented the opportunity to obtain a more accurate estimate of systematic errors induced by different instrumental setups—which might otherwise be masked by apparent internal consistency—and thereby come closer to achieving calibration on a system

consistent with that of high-redshift SNe as required for accurate measurement of the cosmological parameters. Of course, the need to account for the specific characteristics of these many different instruments, and their cross-calibration, made the calibration a particularly challenging component of this analysis, which we have addressed in a unique fashion.

Our photometric calibration procedure is subdivided into three parts:

1. Determination of zero points, color terms, and atmospheric extinction for photometric nights on telescopes at high-quality sites, simultaneously employing observations of both Landolt (1992) standard stars and SN field tertiary standard stars.
2. Use of the tertiary standard stars to simultaneously determine color terms for all other instruments, and zero points for all other images.
3. Determination of SN magnitudes, including the SN host subtraction and photometric correction necessary for nonstandard bandpasses.

In steps 1 and 2 the robustness of the fits was ensured by heavily deweighting significant outliers, using an automated iterative prescription.

Elaborating further on step 1, the instrumental magnitudes were converted to magnitudes on the standard $BV(RI)_{\rm KC}$ system using the relation

$$m_x = \tilde{m}_x + m_{\rm zp} + k_x\chi + c_x(m_x - m_y), \qquad (1)$$

where $\tilde{m}_x$ is the instrumental magnitude measured in band x, m_x and m_y are the apparent magnitudes in bands x and y, χ is the air mass, $m_{\rm zp}$ is the zero point, and k_x and c_x are the atmospheric extinction and filter correction terms for band x. A simultaneous fit in two bands of standard stars cataloged by Landolt (1992) and our SN field stars allowed determination of $m_{\rm zp}$, k_x, χ, and c_x, as well as m_x and m_y for our tertiary standard stars. In total, 125 Landolt standards, spread across 16 photometric nights, were used for calibration in B, V, R, and I, respectively. Accordingly, the uncertainties on the night and telescope-dependent terms k_x and c_x are typically very small. Their covariance with the other parameters is properly accounted for. The catalog of tertiary standard stars generated as a by-product of this procedure are reported in Appendix B.

Then, in step 2, the apparent magnitudes from the tertiary standard stars were used to determine color terms for all remaining instruments and zero points for all images. Since *BVRI* do not require air mass–color cross terms over the range of air masses covered by our observations, and since absorption by any clouds present would be gray, it was possible to absorb the atmospheric extinction into the zero point of each image. The catalog of tertiary standard stars includes both rather blue and red stars, therefore allowing reliable determination of the color terms. The color terms obtained for all instruments are summarized in Table 7 of Appendix A.

In order to determine the counts from the SN in a given aperture, the counts expected from the underlying host galaxy must be subtracted. In our approach, the image with the SN and the reference images without SN light are first convolved to have matching point-spread functions. Stars in the images are used to approximate the PSF as a Gaussian, which for the purposes of determining the convolution kernel needed to match one PSF to another is usually adequate. The instrumental magnitudes of objects (including galaxies) in the field are then used to determine the ratio of counts between the images. For a given image, the counts due to the SN are obtained by subtracting the counts from the reference image scaled by the ratio of counts averaged over all objects. Note that with this approach the images are never spatially translated, thereby minimizing pixel-to-pixel correlations due to resampling.

Several contributions to the uncertainty were evaluated and added in quadrature: photon statistics, uncertainties in the image zero points, and uncertainties in the scaling between reference and SN image. In addition, possible systematic errors introduced during sky subtraction and flat-fielding are evaluated using field stars. The variance of field star residuals is used to rescale all uncertainties. Also, an error floor is determined for all instruments by investigation of the variance of the residuals as a function of the calculated uncertainty. Such an error might occur due to large-scale variation in the flat-field. An appropriate error floor was found to be typically 1%–2% of the signal counts.

2.2. *Bandpass Determination*

The bandpasses for all telescopes have to be established in order to correct for potential mismatches to the Landolt/Bessell system (Landolt 1992; Bessell 1990).

The bandpass is the product of the quantum efficiency of the CCD, the filter transmission curve, the atmospheric transmission, and the reflectivity of the telescope mirrors. Figure 1 shows the bandpass curves for the various instruments used in this work. The relevant data were obtained either from the instrument documentation or through private communication.

We test for consistency of the bandpasses using synthetic photometry (for a related study, see Stritzinger et al. 2002). For this, stellar spectra that best match the published *UBVRI* colors of our standard stars are selected from the catalog of Gunn & Stryker (1983). The spectra that best match the published colors of the standard stars are further adjusted using cubic splines to exactly match the published colors. For instruments without standard star observations, a second catalog is generated using our determination of *BVRI* magnitudes of field stars. With the spectra of standard and field stars at hand, we perform synthetic photometry for the various bandpass functions. The bandpass functions are then shifted in central wavelength by $\Delta\lambda$ until they optimally reproduce the observed instrumental magnitudes. The change in color-term, c_x, when shifting the passband is $dc_x/d\lambda \approx 0.001$, 0.0008, 0.0005, 0.0003 Å^{-1} for B, V, R, and I, respectively. An alternative procedure is to evaluate the color terms for a given bandpass in an analogous way as for the observed magnitudes (see eq. [1]). We then determine the wavelength shift to apply to the bandpasses in order to reproduce the instrumental color terms. The two approaches agree on average to within 1 Å with an rms of about 20 Å. The results are summarized in Table 8 of Appendix A. The associated systematic uncertainty on the photometric zero point due to this shift depends on the color of the object and for $B - V \leq 1$ will remain below 0.02 mag.

3. LIGHT CURVES

3.1. *Light Curves from the SCP Nearby 1999 Supernova Campaign*

Figure 2 shows the *BVRI* light curves from the SCP Nearby 1999 campaign (the data are provided in Table 10). Different telescopes are marked by different symbols. Empty symbols represent uncorrected photometric data, and filled symbols represent data corrected for nonstandard bandpasses, the so-called *S*-corrections (Suntzeff 2000). The *S*-corrections represent the magnitude shift needed to bring the data obtained with different bandpasses to a common standard system (in our case the Bessell system). The *S*-corrections are obtained from a synthetic photometry calculation using the ''instrument-dependent'' bandpass functions

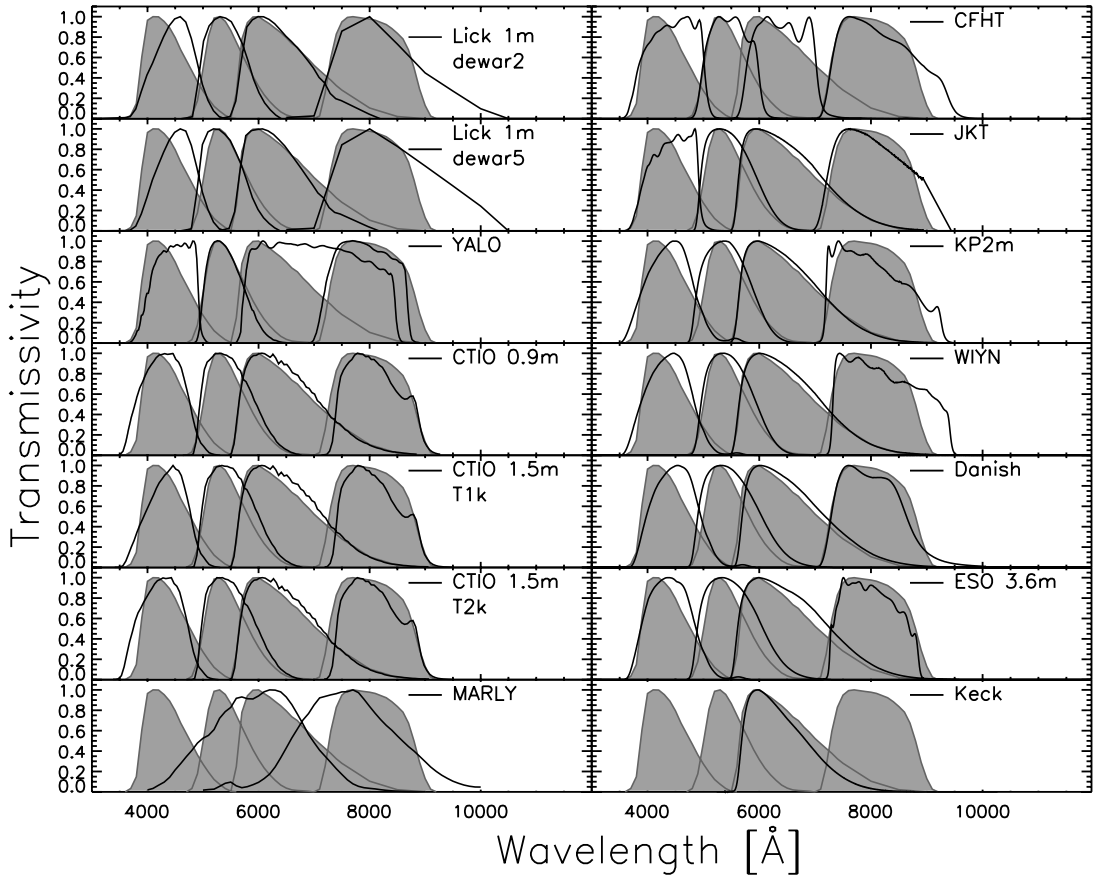

FIG. 1.—Bandpasses for the various instruments used in the Spring 1999 Nearby Supernova Campaign. For comparison, the filled regions represent the passband transmission functions of the Bessell (1990) system.

described above and a spectrophotometric light curve model. The spectrophotometric SN light curve model was adjusted using spline functions to match the colors of the light curve models of our SNe. The light curve models are shown in Figure 2 to guide the eye only. They are obtained in two different ways depending on the quality of the available photometric data. For the four SNe with $z < 0.1$, we have used the fit method explained in Wang et al. (2006), which has six parameters per band. This method allows effective fitting of *R*- and *I*-band data, which exhibits a second "bump" of variable strength appearing approximately 30 days after the maximum. However, since this fit method has six free parameters per fitted band, one can use it only for light curves with dense temporal sampling with high signal-to-noise ratio. For the more distant SNe 1999ar, 1999bi, 1999bm, and 1999bn we use a more constrained light curve fitting method based on template matching. A library of template light curves obtained from well-observed supernovae is *K*-corrected to the observed redshift. The best-matching light curve is chosen as a model for the supernova. The light curve models along with the *S*-corrections shown in Figure 2 are meant to guide the eye and will not be used in the remainder of the paper; we continue with the concept of using instrumental magnitudes along with instrument-dependent passbands when fitting the light curve parameters.

The light curve parameters such as peak magnitude, stretch, and color at maximum are obtained using the spectral template method of Guy et al. (2005), which is described in more detail in § 3.3. The method is well suited to this task since it uses telescope-specific bandpass functions for modeling the observer-frame light curves. The *B*-band (*left*) and *V*-band (*right*) observer-frame light curves are shown in Figure 3, along with the light curves predicted by the spectral template for the corresponding bandpass. In the bottom part of the plots we show the residuals from the model prediction. In most cases the model describes the data reasonably well, with $\chi^2/\mathrm{dof} \sim 1$. Systematic deviations, such as observed in the late-time behavior of the *B*-band light curve of SN 1999aw, are likely to be attributable to the limitations of the two-parameter spectral template model in capturing the full diversity of Type Ia supernovae light curves.

Figure 4 (*right and middle*) shows the fitted $B - V$ color at maximum, as well as the stretch distribution. The stretch distribution has one low-stretch supernova (SN 1999bm) but is otherwise dominated by supernovae with larger stretches. Two lower stretch SNe Ia were found in these searches but are not presented here because of their faintness—in one case combined with proximity to the cuspy core of an elliptical host—prevented an analysis using the techniques described here. In any case, the larger number of high-stretch supernovae is not very significant (a K-S test resulted in a 20% probability that the two distributions are consistent with each other).

For two of the eight supernovae, light curve data have previously been published. Jha et al. (2006), Krisciunas et al. (2000), and Altavilla et al. (2004) presented independent data on SN 1999aa. When comparing the fit results for SN 1999aa we find agreement to within 1% in maximum *B*-band luminosity, color, and stretch. Spectroscopic and photometric data on SN 1999aw were previously reported by Strolger et al. (2002). While the raw data of Strolger et al. (2002) are largely the same as that presented here, the reduction pipelines used are independent. A main difference is the treatment of nonstandard bandpasses. We report the original magnitudes and correct for nonstandard bandpasses during the fit of the light curve, while in Strolger et al.

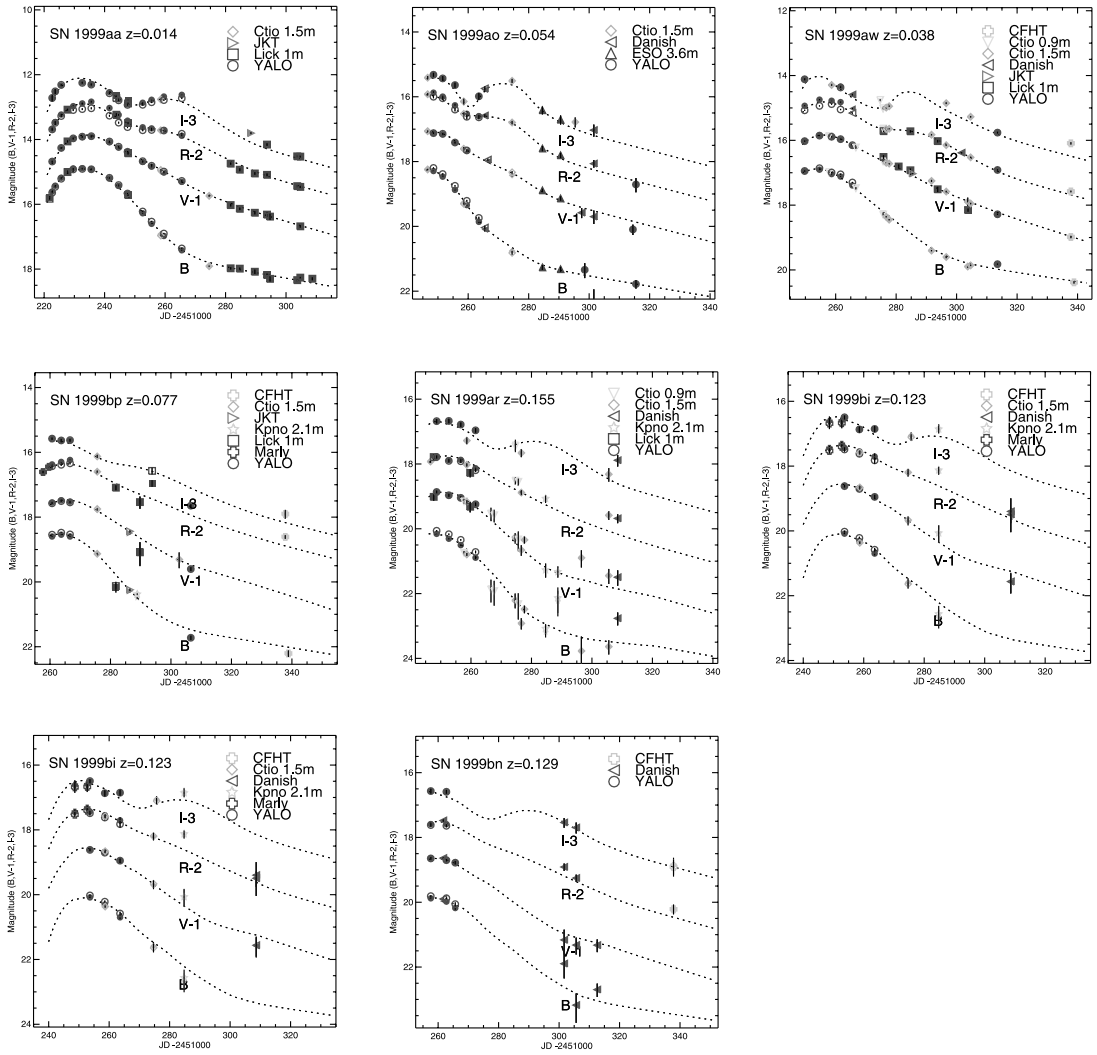

FIG. 2.—SNe light curves of the SCP Nearby 1999 campaign. The filled symbols represent the *S*-corrected data, and the empty symbols the raw photometric data. Both the *S*-corrected data as well as the model parameterization (*dashed line*) are shown to guide the eye only and are not used any further in the remaining paper. [*See the electronic edition of the Journal for a color version of this figure.*]

(2002) corrections based on the color coefficient have been applied to the data. When fitting for peak B-band magnitude, color, and stretch, we obtain differences of $\Delta B = 0.04$, $\Delta(B - V) = 0.02$, and $\Delta s = 0.005$.

Figure 4 (*left*) shows the redshift distribution relative to the sample of other nearby supernovae (see § 3.2 for a definition of that sample). As can be seen, the distribution extends to redshifts $z \sim 0.15$, an underpopulated region in the Hubble diagram.

3.2. *Literature Supernovae*

Here we discuss the set of previously published nearby and distant supernovae included in the analysis. Not all SN light curves are of sufficiently good quality to allow their use in the following cosmological analysis. For all supernovae in the sample, we require that data from at least two bands with rest-frame central wavelength between 3470 Å (U band) and 6600 Å (R band) exist and that there are in total at least five data points available.

Further, we require that there is at least one observation existing between 15 days before and 6 days after the date of maximal B-band brightness, as obtained from an initial fit to the light curves (see § 3.3). The 6 day cut is scaled by stretch for consistency. In addition, we observed that for a smaller number of poorer light curves, the uncertainties resulting from the fits are unphysically small compared to what is expected from the photometric data. In these cases, we randomly perturb each data point by a tenth (or if necessary by a fifth) of its photometric error and refit the light curves. The remaining 16 SNe, where convergence cannot be obtained even after perturbation of the data, are excluded from further analysis (note that these SNe are generally poorly measured and would have low weight in any cosmological analysis).

For the nearby SN sample, we use only supernovae with CMB-centric redshifts $z > 0.015$, in order to reduce the impact of uncertainty due to host galaxy peculiar velocities. We checked that our results do not depend significantly on the value of the redshift cutoff (tested for a range $z = 0.01$–0.03).

The number of SNe passing these cuts are summarized in Table 2. Each individual supernova is listed in Table 11, and the last column indicates any cuts that the supernova failed.

The list contains 17 supernovae from Hamuy et al. (1996), 11 from Riess et al. (1999), 16 from Jha et al. (2006), and 6 from Krisciunas et al. (2004a, 2004b, 2001). Our light curve data for SN 1999aa are merged with that of Jha et al. (2006). To this list of nearby supernovae from the literature we add the new nearby supernovae presented here. For SN 1999aw, we use only the light curve data presented in this paper. Hence, the sample contains 58 nearby supernovae.

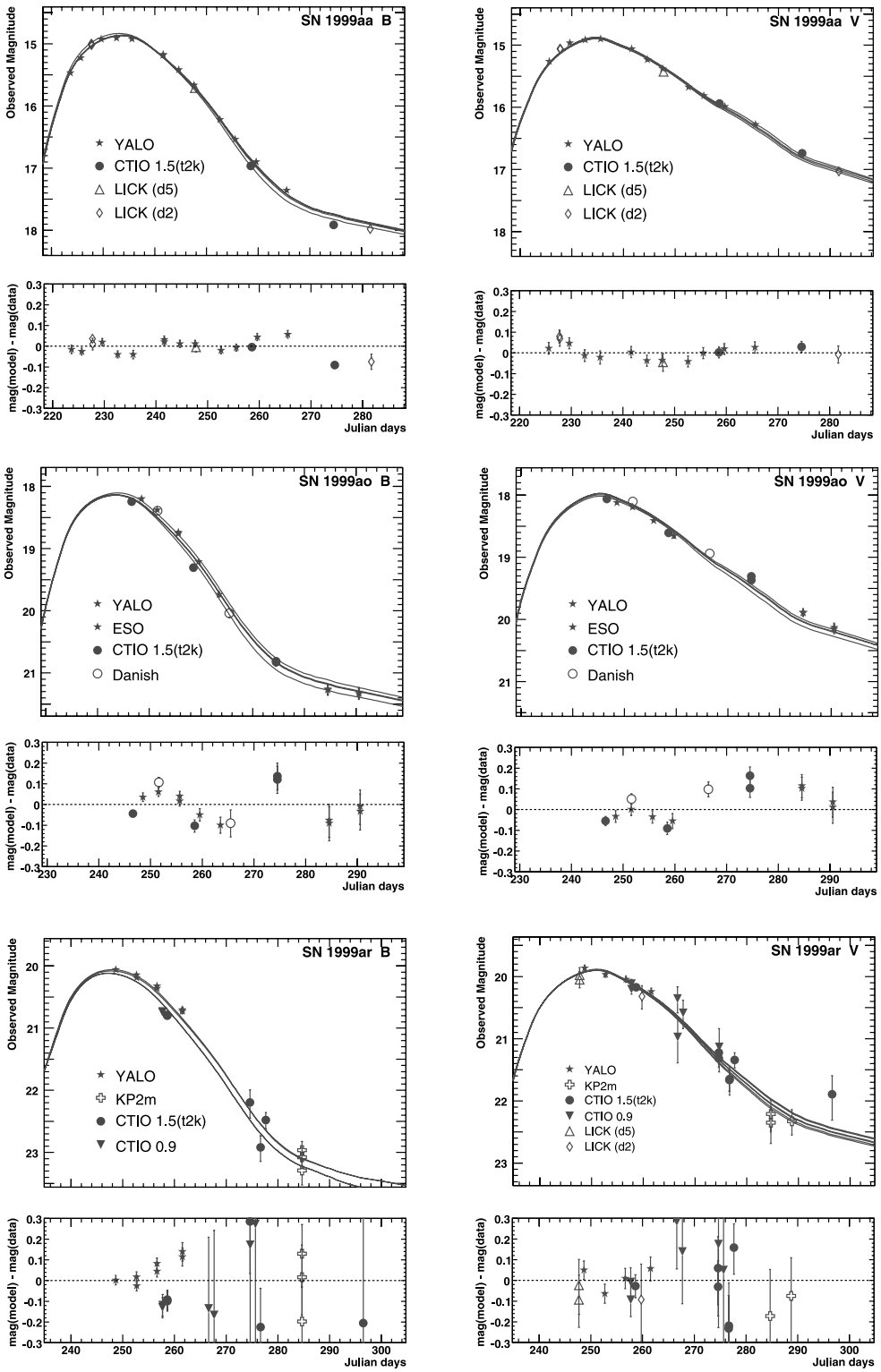

FIG. 3.—*B* and *V* light curves and residuals. The multiple curves represent the model predictions for the different bandpasses and are obtained by integrating the product of passband and the redshifted spectral template. [*See the electronic edition of the Journal for a color version of this figure.*]

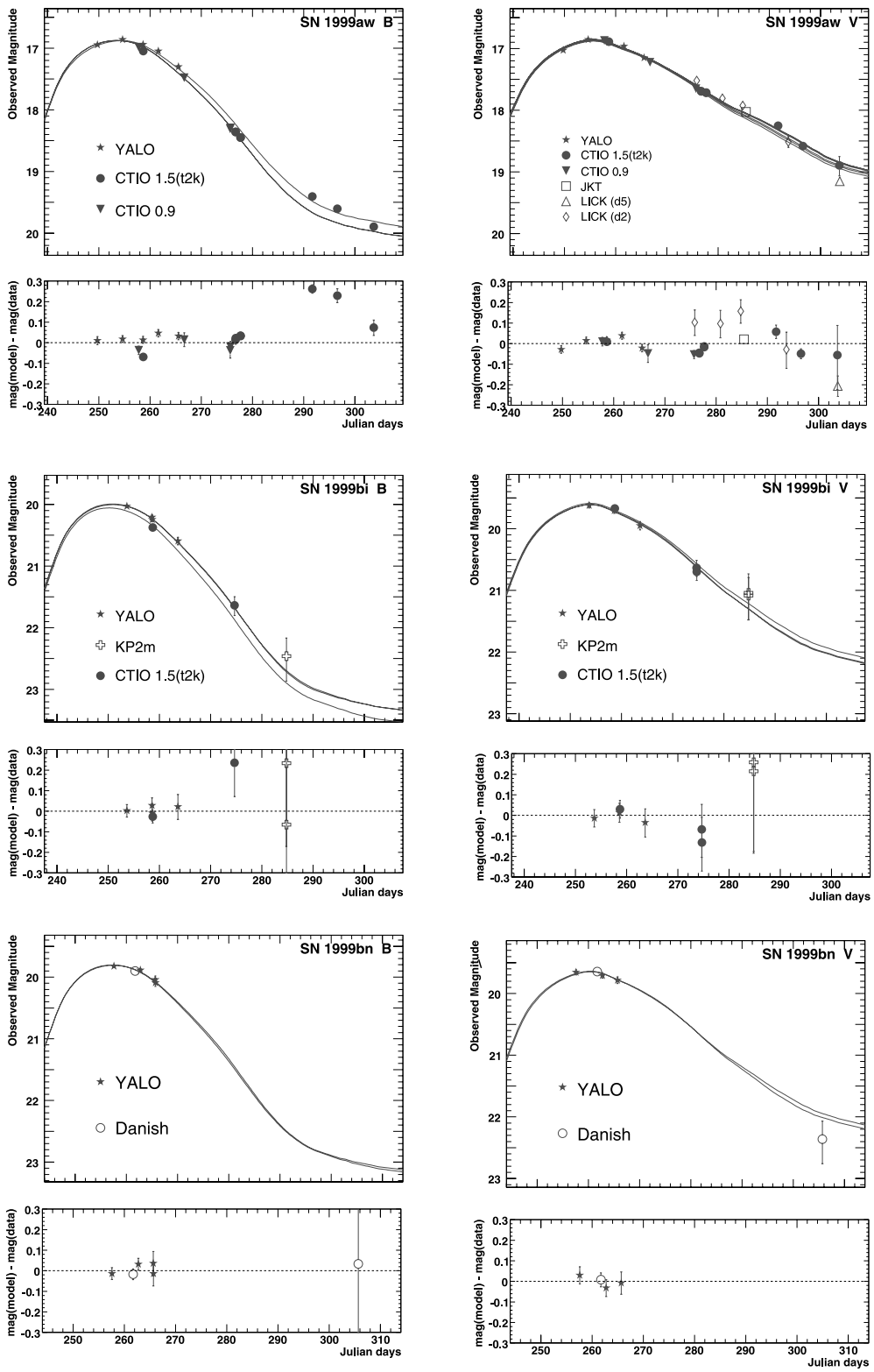

FIG. 3—*Continued*

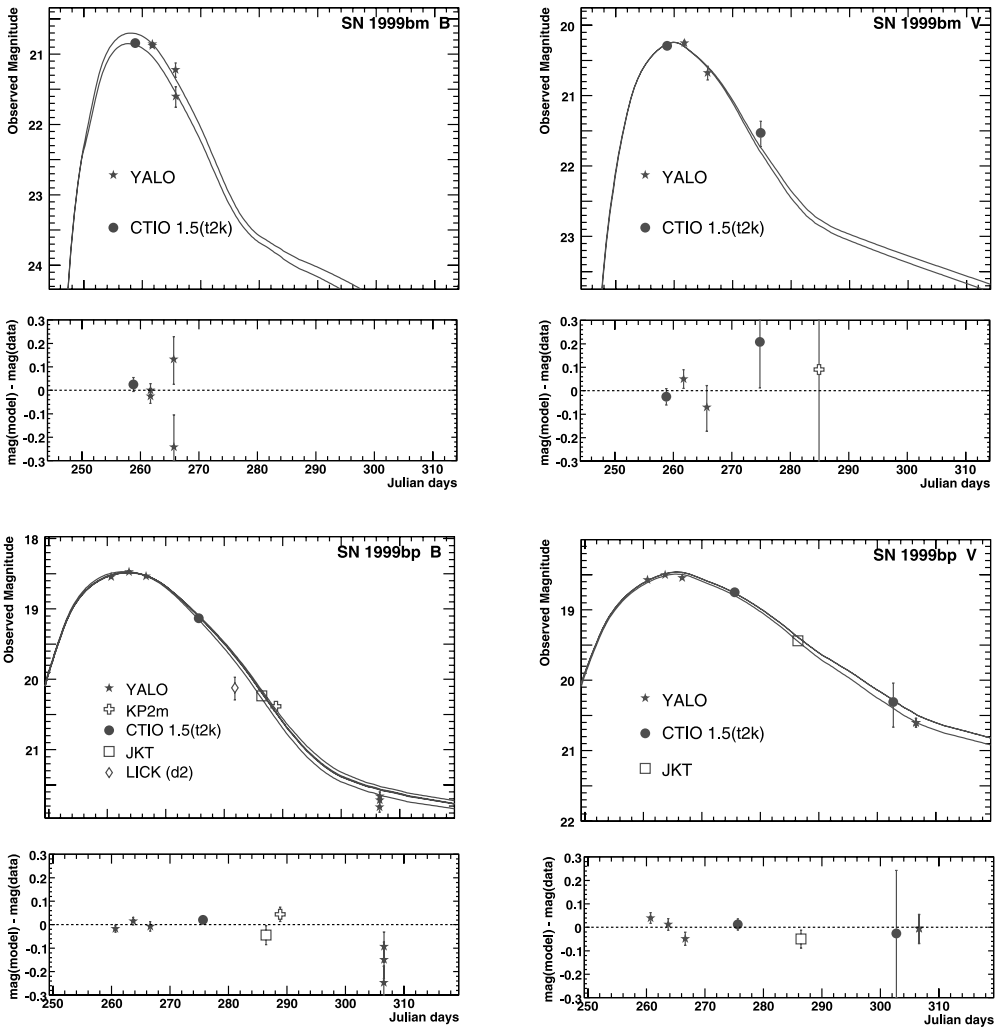

FIG. 3—*Continued*

The sample of high-redshift supernovae is comparably heterogeneous. We use all of the 11 SNe from Knop et al. (2003) that have light curves obtained with *HST*. Of the 42 supernovae from Perlmutter et al. (1999), 30 satisfy the selection cuts described above (as can be seen in the photometry data of Table 12). Of the 16 SNe used by the High-Z Team (HZT; Riess et al. 1998; Garnavich et al. 1998; Schmidt et al. 1998), two are already included in the Perlmutter et al. (1999) sample, and of the remaining 14, 12 pass our cuts.

Included also are 22 SNe from Barris et al. (2004) and the 8 SNe from Tonry et al. (2003) that are typed to be secure or likely SNe Ia. We do not use SN 1999fv and SN 1999 fh, as the

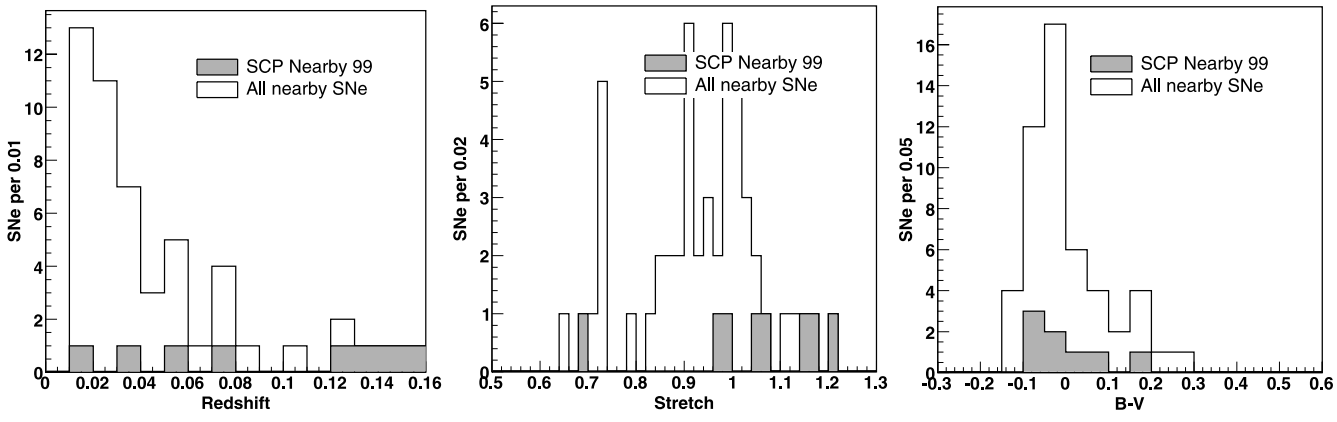

FIG. 4.—*Left*: Redshift distribution; *middle*: stretch distribution; *right*: $B - V|_{t=B_{\max}}$ distribution.

TABLE 2
Number of Supernovae after Consecutive Application of Cuts

Requirement	N_{SN}
All	414
$z > 0.015$	382
Fit successful	366
Color available	351
First phase <6 days	320
≥5 data points	315
Outlier rejection	307

Note.—See § 4.3 for a discussion of the outlier rejection cut.

number of available data points does not exceed the number of light curve fit parameters.

We add the 73 SNe Ia from the first year of SNLS (Astier et al. 2006), of which one does not pass the first phase cut (03D3cc). Note that in Astier et al. (2006) 2 of the 73 supernovae were excluded from their cosmological parameter fits because they were significant outliers (see discussion in § 4.3). Riess et al. (2004, 2007) have published 37 supernovae that were discovered and followed using *HST*. Of these, 29 passed our light curve quality cuts. This sample contains the highest-redshift supernovae in our compilation. Finally, we use the 84 SNe from the ESSENCE survey (Miknaitis et al. 2007; Wood-Vasey et al. 2007), of which 75 pass our cuts.

3.3. *Light Curve Fitting*

The spectral-template–based fit method of Guy et al. (2005), also known as SALT, is used to fit consistently both new and literature light curve data. This method is based on a spectral template (Nugent et al. 2002) that has been adapted in an iterative procedure to reproduce a training set of nearby SNe *UBVR* light curve data. The training set consists of mostly $z < 0.015$ SNe and hence does not overlap with the sample we use for determination of cosmological parameters. To obtain an expected magnitude for a supernova at a certain phase, the model spectrum is first redshifted to the corresponding redshift followed by an integration of the product of spectrum and bandpass transmission. The spectral-template–based fit method has the advantage that it consistently allows the simultaneous fit of multiband light curves with arbitrary (but known) bandpass transmission functions. In view of the large number of filters and instruments used for the new nearby SN samples as well as the very diverse light curve data found in the literature, this is particularly important here. In addition, frequent practical problems associated with *K*-corrections—such as the propagation of photometric errors—are handled naturally.

The spectral template based fit method of Guy et al. (2005) fits for the time of maximum, the flux normalization as well as rest-frame color at maximum defined as $c = B - V|_{t=B_{\max}} + 0.057$ and timescale stretch s. It is worth noting that by construction, the stretch in SALT has a related meaning to the conventional time-axis stretch (Perlmutter et al. 1997; Goldhaber et al. 2001). However, as a parameter of the light curve model it also absorbs other, less pronounced, stretch-dependent light curve dependencies. The same is true for the color c.

Recently, direct comparisons between alternative fitters, such as SALT, its update (Guy et al. 2007), and MLCS2k2 (Jha et al. 2007) show good consistency between the fit results, e.g., the amount of reddening (Conley et al. 2007). Our own tests have shown that for well-observed supernovae, the method produces very consistent results (peak magnitude, stretch) when compared to the more traditional method of using light-curve templates (Perlmutter et al. 1997). However, we noticed that fits of poorly observed light curves in some cases do not converge properly. Part of the explanation is that in the case of the spectral template based fit method, the data before $t < -15$ days are not used as an additional constraint. More typically, the SALT fitter can fall into an apparent false minimum, and we then found it necessary to restart it repeatedly to obtain convergence. Note that the small differences between the light curve fit parameters of Table 11 and the values shown in Table 10 of Wood-Vasey et al. (2007) are primarily cases where the Wood-Vasey et al. (2007) SALT fit did not converge (some of which are noted in Wood-Vasey et al. 2007) and a few cases where we found it necessary to remove an extreme outlier photometry point from the light curve.

The light curves from Barris et al. (2004) and the *I*-band light curves of 4 supernovae of P99 (SNe 1997O, 1997Q, 1997R, and 1997am; see also Knop et al. 2003) need a different analysis procedure, since in these cases the light of the host galaxy was not fully subtracted during the image reduction. We hence allow for a constant contribution of light from the host galaxy in the light curve fits. The supernovae were fitted with additional parameters: the zero level of the *I*-band light curve in the case of the four SNe from the P99 set and the zero level of all the bands in the case of the Tonry et al. (2003) data. The additional uncertainties due to these unknown zero levels have been propagated into the resulting light curve fit parameters.

The fitted light curve parameters of all SNe can be found in Table 11.[42]

4. HUBBLE DIAGRAM CONSTRUCTION AND COSMOLOGICAL PARAMETER FITTING

The full set of light curves as described in § 3.2 have been fitted, yielding B-band maximum magnitude $m_B^{\max}$, stretch s, and color $c = B - V|_{t=B_{\max}} + 0.057$. In this section, these are input to the determination of the distance modulus. The analysis method is chosen to minimize bias in the estimated parameters (see § 4.2). An outlier rejection based on truncation is performed that is further described in § 4.3, before constraints on the cosmological parameters are computed.

4.1. *Blind Analysis*

Following Conley et al. (2006) we adopt a blind analysis strategy. The basic aim of pursuing a blind analysis is to remove potential bias introduced by the analyst. In particular, there is a documented tendency (see, e.g., Yao et al. 2006) for an analysis to be checked for errors in the procedure (even as trivial as bugs in the code) up until the expected results are found but not much beyond. The idea of a blind analysis is to hide the experimental outcome until the analysis strategy is finalized and debugged. However, one does not want to blind oneself entirely to the data, as the analysis strategy will be partially determined by the properties of the data. The following blindness strategy is used, which is similar to the one invented in Conley et al. (2006). The data are fit assuming a ΛCDM cosmology, with the resulting fit for Ω_M stored without being reported. The flux of each supernova data point is then rescaled according to the ratio of luminosity distances obtained from the fitted parameters and arbitrarily chosen dummy parameters (in this case $\Omega_M = 0.25,\ \Omega_\Lambda = 0.75$). This procedure preserves the stretch and color distribution and, as

[42] See http://supernova.lbl.gov/Union.

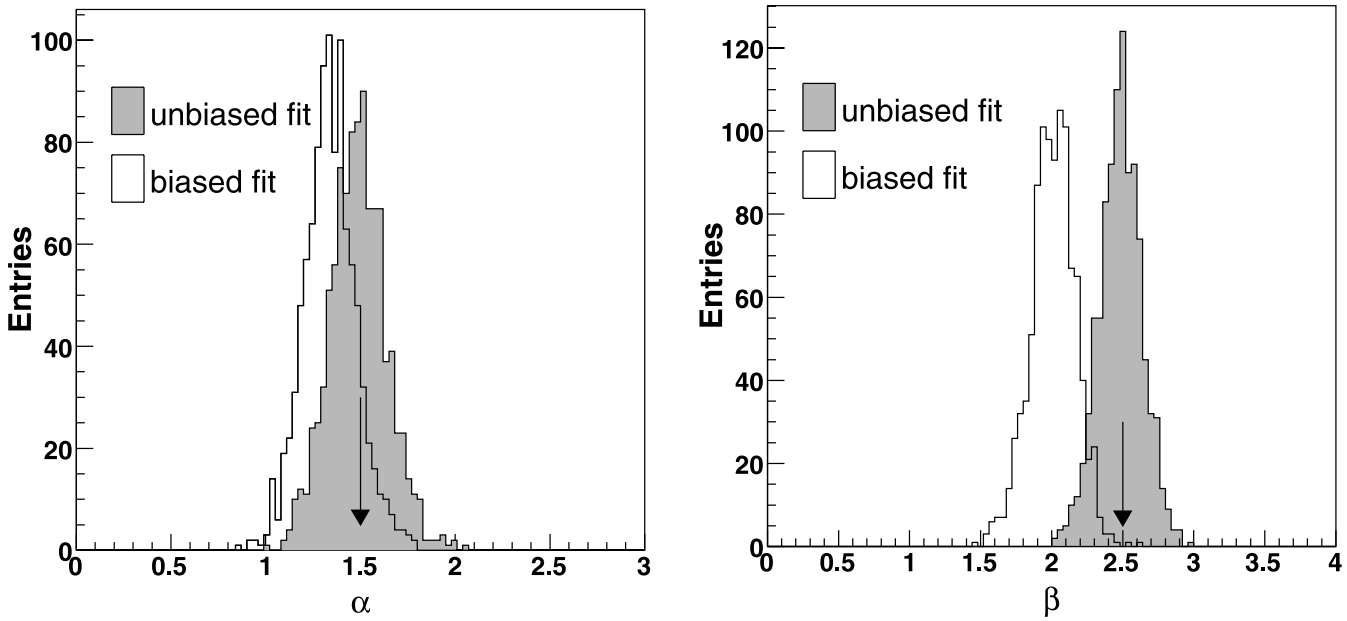

FIG. 5.—Monte Carlo simulation of the resulting α (*left*) and β (*right*) distributions as fitted with the unbiased and biased method. The true values $\alpha = 1.5$ and $\beta = 2.5$ are represented by the arrows.

long as the fitted parameters are not too different from the target parameters, approximately preserves the residuals from the Hubble diagram. In developing the analysis, one is only exposed to data blinded by the procedure described above. Only after the analysis is finalized and the procedure frozen is the blinding turned off.

Note that this prescription allows—in a consistent way—the inclusion of future data samples. A new data sample would be first investigated in a blind manner following the tests outlined in § 4.4, and if no anomalies are observed, one would combine it with the other data sets.

4.2. *Unbiased Parameter Estimation*

Type Ia supernovae obey a redder-dimmer relation and a wider-brighter relation (Phillips 1993). The redder-dimmer relation in principle can be explained by dust extinction; however, the total to selective extinction ratios generally obtained empirically are smaller than expected from Milky-Way–like dust (Tripp 1998; Tripp & Branch 1999; Parodi et al. 2000; Guy et al. 2005; Wang et al. 2006). At the same time, the exact slope of the stretch-magnitude relation is not (yet) predicted by theory. The absence of a strong theoretical prediction motivates an empirical treatment of stretch and color corrections. Here we adopt the corrections of Tripp (1998; see also Tripp & Branch 1999; Wang et al. 2006; Guy et al. 2005; Astier et al. 2006):

$$\mu_B = m_B^{\max} - M + \alpha(s-1) - \beta c. \tag{2}$$

Since the β-color correction term must account for both dust and any intrinsic color-magnitude relation, it is clearly an empirical approximation. The validity of β-color correction relies on only one assumption—that is, nearby supernovae and distant supernovae have an identical magnitude-color relation. If either the intrinsic SNe properties or the dust extinction properties of the supernovae are evolving with redshift, these assumptions may be violated. Observational selection effects may also introduce biases that invalidate equation (2). These potential sources of systematic error will be evaluated in § 5.1.

The χ^2 corresponding to that of equation (2) is given as

$$\chi^2 = \sum\nolimits_{\rm SNe} \frac{[\mu_B - \mu(z, \Omega_M, \Omega_\Lambda, w)]^2}{\sigma_{\rm tot}^2 + \sigma_{\rm sys}^2 + \sum_{ij} c_i c_j C_{ij}}. \tag{3}$$

The sum in the denominator represents the statistical uncertainty as obtained from the light-curve fit with C_{ij} representing the covariance matrix of fitted parameters: peak magnitudes, color, and stretch (i.e., $C_{11} = \sigma_{m_B}^2$) and $c_i = \{1, \alpha, -\beta\}$ are the corresponding correction parameters.

The quantity $\sigma_{\rm tot}$ represents an astrophysical dispersion obtained by adding in quadrature the dispersion due to lensing, $\sigma_{\rm lens} = 0.093z$ (see § 5.6), the uncertainty in the Milky-Way dust extinction correction (see § 5.8), and a term reflecting the uncertainty due to host galaxy peculiar velocities of 300 km s^{-1}. The dispersion term $\sigma_{\rm sys}$ contains an observed sample-dependent dispersion due to possible unaccounted-for systematic errors. In § 4.3 we discuss the contribution of $\sigma_{\rm sys}$ further.

Note that equation (3) can be derived using minimization of a generalized χ^2. Defining a residual vector for a supernova $\boldsymbol{R} = (\mu_B - \mu_{\rm model},\ s - s',\ c - c')$ and supposing that the light-curve fit returns covariance matrix $\mathbf{C}$, we can write

$$\chi^2 = \sum\nolimits_{\rm SNe} \boldsymbol{R}^T \mathbf{C}^{-1} \boldsymbol{R}. \tag{4}$$

Here s' and c' take the role of the true stretch and color, which have to be estimated from the measured ones. Minimizing this equation over all possible values of s' and c' gives the χ^2 in equation (3). The χ^2 is minimized, not marginalized, over α and β; marginalization would yield a biased result due to the asymmetry of the χ^2 about the minimum.

Frequently, equation (3) is minimized by updating the denominator iteratively, i.e., only between minimizations (see, e.g., Astier et al. 2006). As shown in Figure 5 and discussed next, this method produces biased fit results, an artifact previously noted by Wang et al. (2006).

We use a Monte Carlo simulation to estimate any biases from the fitting procedure. Random supernova samples resembling

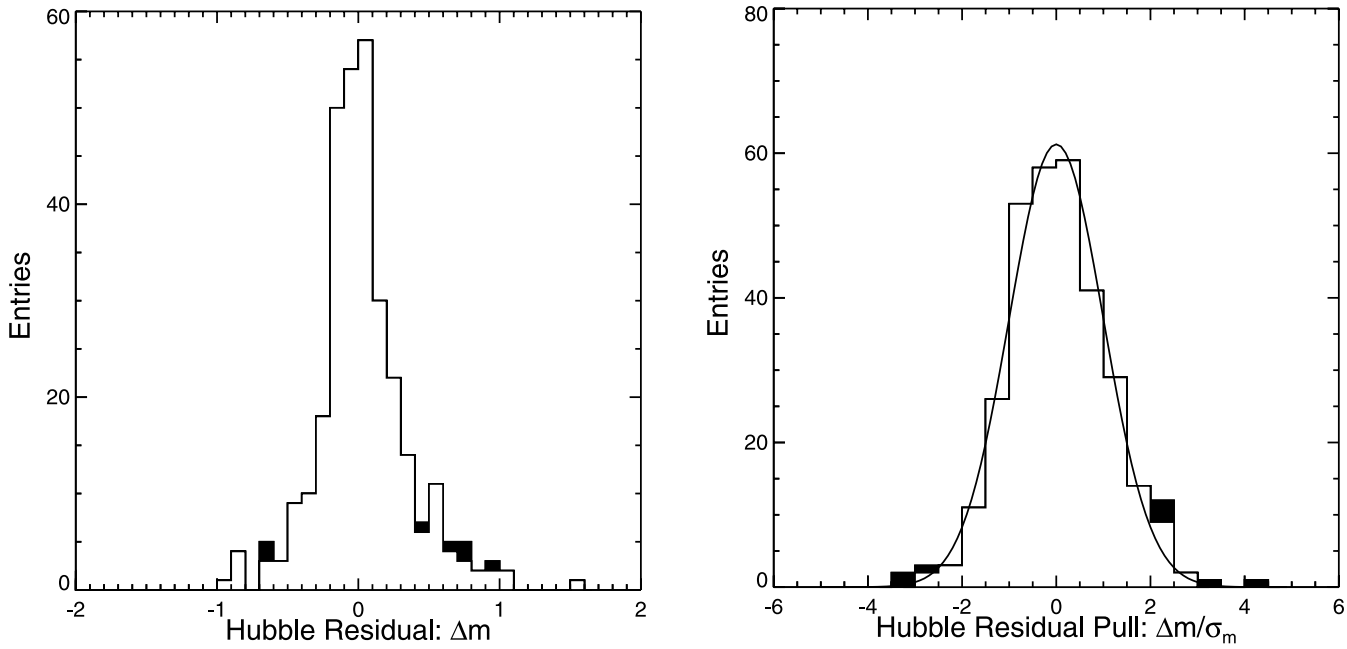

FIG. 6.—Residual of rest-frame, stretch and color-corrected, *B*-band magnitude (*left*) and pull distribution (*right*) from the best-fitting cosmology. The filled histogram shows the rejected outliers. The pull distribution is overlaid with a normal distribution of unit width.

the observed one are generated and then fitted. The true stretch and color are sampled from a normal distribution of width 0.1 and for the peak magnitude an intrinsic dispersion of 0.15 mag is assumed. A further dispersion corresponding to the measurement errors is added. By construction, the SN samples have the same redshift and stretch, color, and peak magnitude uncertainties as the real sample. The test values for α and β were chosen as 1.5 and 2.5. This bias on α and β, as would be obtained from the iterative method's fits to the simulated data sets, is visible in Figure 5 as the unshaded histogram. The large potential bias on β ($\Delta\beta \sim -0.5$), if the χ^2 had been chosen according to equation (3) with the iteratively updated denominator, is a result of the fact that the measurement error on c for high-redshift SNe is similar to and often even exceeds the width of the color distribution itself.

We have investigated other sources of bias in the fitted parameters. A measurement bias will be introduced because overall, brighter SNe will have smaller photometric errors, and hence larger weights, than dimmer ones. If the photometric error bars are small enough that the intrinsic dispersion dominates the uncertainty, this bias will be small. Hence, low-redshift, well-observed SNe are biased less than high-redshift, poorly observed SNe, resulting in biased cosmological parameters. This bias was studied using the Monte Carlo simulation described above. For the sample under investigation we found a bias $\delta M = 0.01$ had been introduced. In principle this bias can be corrected; however, since it is roughly a factor of 3 smaller than the statistical or systematic uncertainties, we chose not to carry out this step.

4.3. *Robust Statistics*

Figure 6 shows the distribution of rest-frame *B*-band corrected magnitude residuals (*left*) from the best fit as obtained with the full data set. The right plot shows the pull distribution, where the pull is defined as the corrected *B* magnitude residual divided by its uncertainty. The distributions have outliers that, if interpreted as statistical fluctuations, are highly improbable. Hence, these outliers point to non-Gaussian behavior of the underlying data, due to either systematic errors in the observations, contamination, or intrinsic variations in Type Ia SNe. The fact that an outlier is present even in the high-quality SNLS supernova set (see Table 3) suggests that contamination or unmodeled intrinsic variations might be present. However, other samples that typically were observed with a more heterogeneous set of telescopes and instruments show larger fractions of outliers, indicating additional potential observation-related problems.

In order to limit the influence of outliers, we use a robust analysis technique. First, the SN samples are fitted for *M*, the absolute magnitude of the SNe, using median statistics (see Gott et al. 2001 for a discussion of median statistics in the context of SN cosmology). The quantity minimized is $\chi = \sum_{\rm SNe}(|\mu_B - \mu_{\rm model}|/\sigma)$, where the uncertainty σ in the denominator includes the covariance terms in the denominator of the right-hand side of equation (3). We then proceed to fit each sample by itself using the α, β, and Ω_M from the combined fit, as χ is not a well-behaved quantity for small numbers of SNe.

For each sample, we remove SNe with a pull exceeding a certain value $\sigma_{\rm cut}$ relative to the median fit of the sample. Currently available algorithms, which correct the peak magnitude using, e.g., stretch or Δm_{15}, are capable of standardizing SNe Ia to a level of $\sim$0.10–0.15 mag. To reflect this we add in quadrature a systematic dispersion to the known uncertainties. The list of known uncertainties include observational errors, distance modulus uncertainties due to peculiar velocities (with $\Delta v = 300$ km s^{-1}) and gravitational lensing (relevant only for the highest-redshift SNe; see § 5.6 for a discussion). The additional systematic dispersion has two components: a common irreducible one, possibly associated with intrinsic variations in the SN explosion mechanism, as well as an observer-dependent component. To obtain self-consistency the systematic dispersion is recalculated during the analysis. One starts by assuming a systematic dispersion of $\sigma_{\rm sys} = 0.15$ magnitudes, then computes the best-fitting cosmology for the particular sample using median statistics, removes the outlier SNe with residuals larger than a cut value $\sigma_{\rm cut}$, iterates $\sigma_{\rm sys}$ such that the total χ^2 per degree of freedom is unity, and in a final step redetermines the best-fitting cosmology using regular χ^2 statistics to obtain an updated $\sigma_{\rm sys}$. From that point in the

TABLE 3

Number of Supernovae Passing the Different Outlier Rejection Cuts, and Sample-dependent Systematic Dispersion (σ_{sys}) and rms around the Best-Fit Model

	No Outlier Cut			$\sigma_{cut} = 3$			$\sigma_{cut} = 2$		
Set	SNe	σ_{sys}(68%)	rms (68%)	**SNe**	σ_{sys}(68%)	**rms** (68%)	SNe	σ_{sys}(68%)	rms (68%)
Hamuy et al. (1996)	17	$0.14^{+0.04}_{-0.03}$	$0.16^{+0.03}_{-0.03}$	**17**	$0.14^{+0.04}_{-0.03}$	$0.16^{+0.03}_{-0.03}$	16	$0.12^{+0.05}_{-0.03}$	$0.15^{+0.02}_{-0.03}$
Krisciunas et al. (2005)	6	$0.06^{+0.11}_{-0.05}$	$0.10^{+0.03}_{-0.04}$	**6**	$0.05^{+0.11}_{-0.05}$	$0.10^{+0.03}_{-0.04}$	6	$0.08^{+0.12}_{-0.07}$	$0.12^{+0.03}_{-0.04}$
Riess et al. (1999)	11	$0.16^{+0.07}_{-0.04}$	$0.18^{+0.03}_{-0.04}$	**11**	$0.16^{+0.07}_{-0.03}$	$0.17^{+0.03}_{-0.04}$	11	$0.18^{+0.08}_{-0.04}$	$0.20^{+0.04}_{-0.05}$
Jha et al. (2006)	16	$0.30^{+0.09}_{-0.05}$	$0.31^{+0.05}_{-0.06}$	**15**	$0.26^{+0.08}_{-0.05}$	$0.27^{+0.05}_{-0.06}$	11	$0.10^{+0.08}_{-0.06}$	$0.15^{+0.03}_{-0.04}$
This work	8	$0.01^{+0.06}_{-0.01}$	$0.09^{+0.02}_{-0.03}$	**8**	$0.00^{+0.05}_{-0.00}$	$0.07^{+0.02}_{-0.02}$	8	$0.07^{+0.06}_{-0.03}$	$0.12^{+0.03}_{-0.04}$
Riess et al. (1998)+HZT	12	$0.29^{+0.20}_{-0.11}$	$0.50^{+0.09}_{-0.12}$	**12**	$0.28^{+0.19}_{-0.10}$	$0.48^{+0.09}_{-0.11}$	10	$0.16^{+0.19}_{-0.10}$	$0.49^{+0.10}_{-0.13}$
Perlmutter et al. (1999)	30	$0.43^{+0.13}_{-0.09}$	$0.65^{+0.08}_{-0.09}$	**29**	$0.33^{+0.10}_{-0.07}$	$0.50^{+0.06}_{-0.07}$	24	$0.19^{+0.11}_{-0.09}$	$0.43^{+0.06}_{-0.07}$
Tonry et al. (2003)	6	$0.00^{+0.33}_{-0.00}$	$0.24^{+0.06}_{-0.09}$	**6**	$0.06^{+0.28}_{-0.06}$	$0.24^{+0.06}_{-0.09}$	6	$0.00^{+0.32}_{-0.00}$	$0.26^{+0.07}_{-0.09}$
Barris et al. (2004)	22	$0.31^{+0.12}_{-0.07}$	$0.64^{+0.09}_{-0.11}$	**21**	$0.23^{+0.12}_{-0.08}$	$0.62^{+0.09}_{-0.10}$	19	$0.11^{+0.16}_{-0.11}$	$0.71^{+0.11}_{-0.13}$
Knop et al. (2003)	11	$0.10^{+0.08}_{-0.04}$	$0.17^{+0.03}_{-0.04}$	**11**	$0.10^{+0.07}_{-0.04}$	$0.17^{+0.03}_{-0.04}$	11	$0.11^{+0.08}_{-0.05}$	$0.18^{+0.04}_{-0.04}$
Riess et al. (2007)	29	$0.22^{+0.05}_{-0.04}$	$0.31^{+0.04}_{-0.04}$	**27**	$0.16^{+0.05}_{-0.04}$	$0.26^{+0.03}_{-0.04}$	24	$0.08^{+0.05}_{-0.06}$	$0.22^{+0.03}_{-0.03}$
Astier et al. (2006)	72	$0.14^{+0.03}_{-0.02}$	$0.31^{+0.03}_{-0.03}$	**71**	$0.12^{+0.03}_{-0.02}$	$0.29^{+0.02}_{-0.03}$	70	$0.12^{+0.03}_{-0.02}$	$0.30^{+0.02}_{-0.03}$
Miknaitis et al. (2007)	75	$0.21^{+0.04}_{-0.03}$	$0.32^{+0.02}_{-0.03}$	**73**	$0.18^{+0.04}_{-0.03}$	$0.30^{+0.02}_{-0.03}$	66	$0.00^{+0.05}_{-0.00}$	$0.23^{+0.02}_{-0.02}$
Union	315			**307**			282		

Note.—The compilation obtained with the $\sigma_{cut} = 3$ cut will be referred to as the Union robust set.

analysis, after outliers are rejected and σ_{sys} determined, only regular χ^2 statistics are applied.

When using a robust analysis, it is necessary to check that (1) in the absence of contamination the results are not altered from the Gaussian case and (2) in the presence of a contaminating contribution, its impact is indeed reduced. In order to investigate this, we begin with a model for the contamination. We assume the data sample to be composed of two types of objects, one representing the desired SNe Ia and a second contribution characterizing the contamination. We then use a maximum-likelihood analysis of the observed pull distribution shown in Figure 6 (*right*) to determine the normalization, width and mean of the contaminating distribution. The uncontaminated pull distribution is assumed to be a Gaussian distribution of unit width and zero mean. The observed pull distribution is best-fitted by an additional contaminating contribution that is 50% wider ($\sigma_m = 0.23$ mag) and that has a mean shifted by $\Delta m = 0.3\sigma_m$, normalized to 18% of the area. A mock simulation that is based on this superposition of two normal distributions illustrates the benefits of using the robust analysis. Figure 7 (*right*) shows the bias of the mean relative to the center of the main component as a function of the outlier rejection cut value. Outlier rejection can reduce the bias by a factor of 3 with a remaining bias of less than 0.01 mag. Even for a wide range of contaminant parameters ($\sigma_m = 0.15$–2; $\Delta m = 0$–2 mag) the bias obtained for the robust analysis remains below 0.015 mag. Only in cases where the contamination is larger than 30% does the outlier rejection algorithm become unstable.

Besides reducing the potential bias due to contamination, robust statistics can also lead to tighter parameter constraints through reduction of the intrinsic dispersion. The right panel of Figure 7 shows for the simulated data the average standard deviation as a function of the outlier rejection cut for the 16% contamination case described above. As a reference, the case of a single uncontaminated population of SNe is shown as well. Note that a cut at 3 σ reduces the dispersion noticeably in the case of a contaminated sample, while the uncontaminated single population is affected negligibly (the standard deviation is reduced by 1.3%, e.g., from 0.15 to 0.148 mag).

For the real data, we consider two values $\sigma_{cut} = 2,\ 3$ as well as the case in which all SNe are kept. We chose as our main cut value $\sigma_{cut} = 3$ since, after application of the outlier rejection, standard χ^2 statistics is still a good approximation while at the same time a potential bias introduced by contamination is significantly reduced. Note also that the impact of individual SNe that have residuals close to σ_{cut} is small for large statistics: an additional SN will shift the mean distance modulus of N_{SNe} by at most $\sigma_{cut}\, N_{SNe}^{-1/2}$ standard deviations. Hence, for $N_{SNe} \gtrsim 10$ and $\sigma_{cut} = 3$ the algorithm can be considered stable relative to fluctuations of individual SNe.

4.4. *Sample Characteristics, Dispersion, and Pull*

Figure 8 illustrates the heterogeneous character of the samples. It shows the Hubble and residual diagrams for the various samples, as well as the histogram of the SN residuals and pulls from the best fit. The difference in photometric quality is illustrated in the rightmost column of Figure 8, by showing the error on the color measurement. As can be seen, some samples show a significant redshift-dependent gradient in the errors, while others have small, nearly constant errors (most notably the sample of Knop et al. 2003). The sample of Astier et al. (2006) shows a small color uncertainty up to $z \leq 0.8$ and degrades significantly once the color measurement relies on the poorer z-band data (cf. SALT2 [Guy et al. 2007], which is capable of incorporating light curve data bluer than rest-frame U).

Our analysis is optimized for large, multicolor samples such as that of Astier et al. (2006), since these now dominate the total sample. There is often a better analysis approach for any given specific sample that would emphasize the strengths of that sample's measurements and yield a tighter dispersion and more statistical weight. However, for this combined analysis of many samples it was more important to use a single uniform analysis for every sample, at the cost of degrading the results for some of the smaller samples. This particularly affects some of the very earliest samples, such as Riess et al. (1998), Perlmutter et al. (1999), and Barris et al. (2004), where the color measurements had originally been used with different priors concerning the dust distribution. Treating these samples with the current analysis thus gives significantly larger dispersions (and hence less weight) to these samples than their original analyses. As a check, we have verified that by repeating the analysis according to Perlmutter et al. (1999) we reproduce the original dispersions.

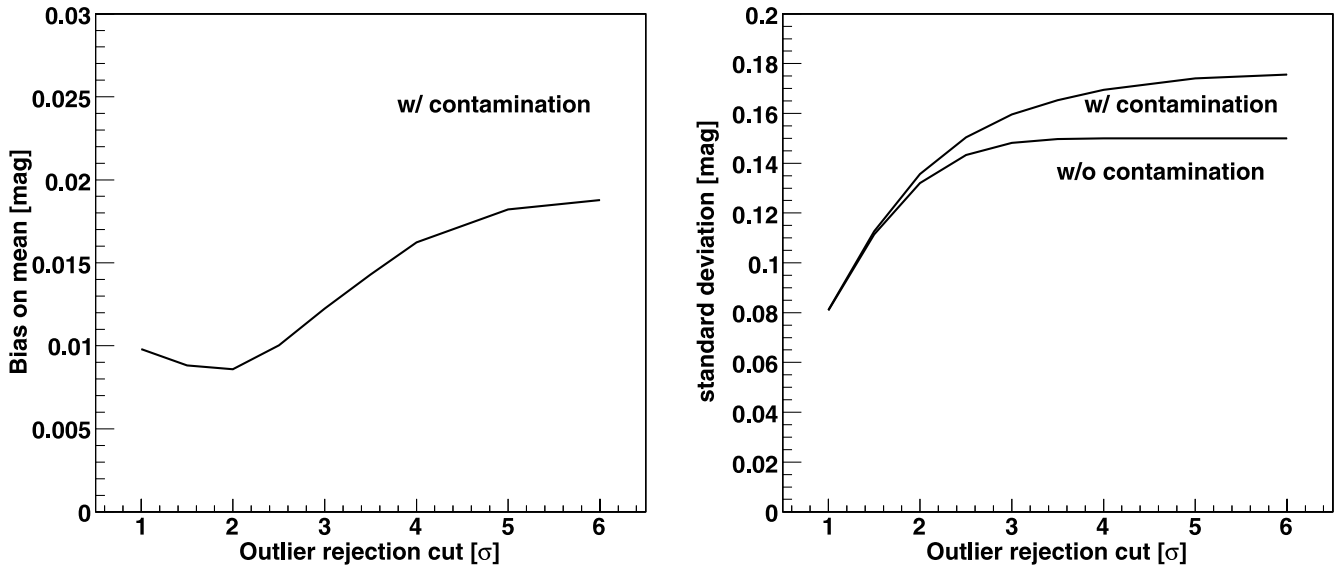

FIG. 7.—Mock simulation of bias (*left*) and standard deviation (*right*) of the mean magnitude as a function of the outlier rejection cut. The simulated SN set consists of one population of 270 SNe with intrinsic dispersion of 0.15 mag and zero mean and a second population of 50 SNe with intrinsic dispersion of 0.26 mag and mean 0.13 mag. The effect of outlier rejection on a single population without contamination is shown as a reference curve.

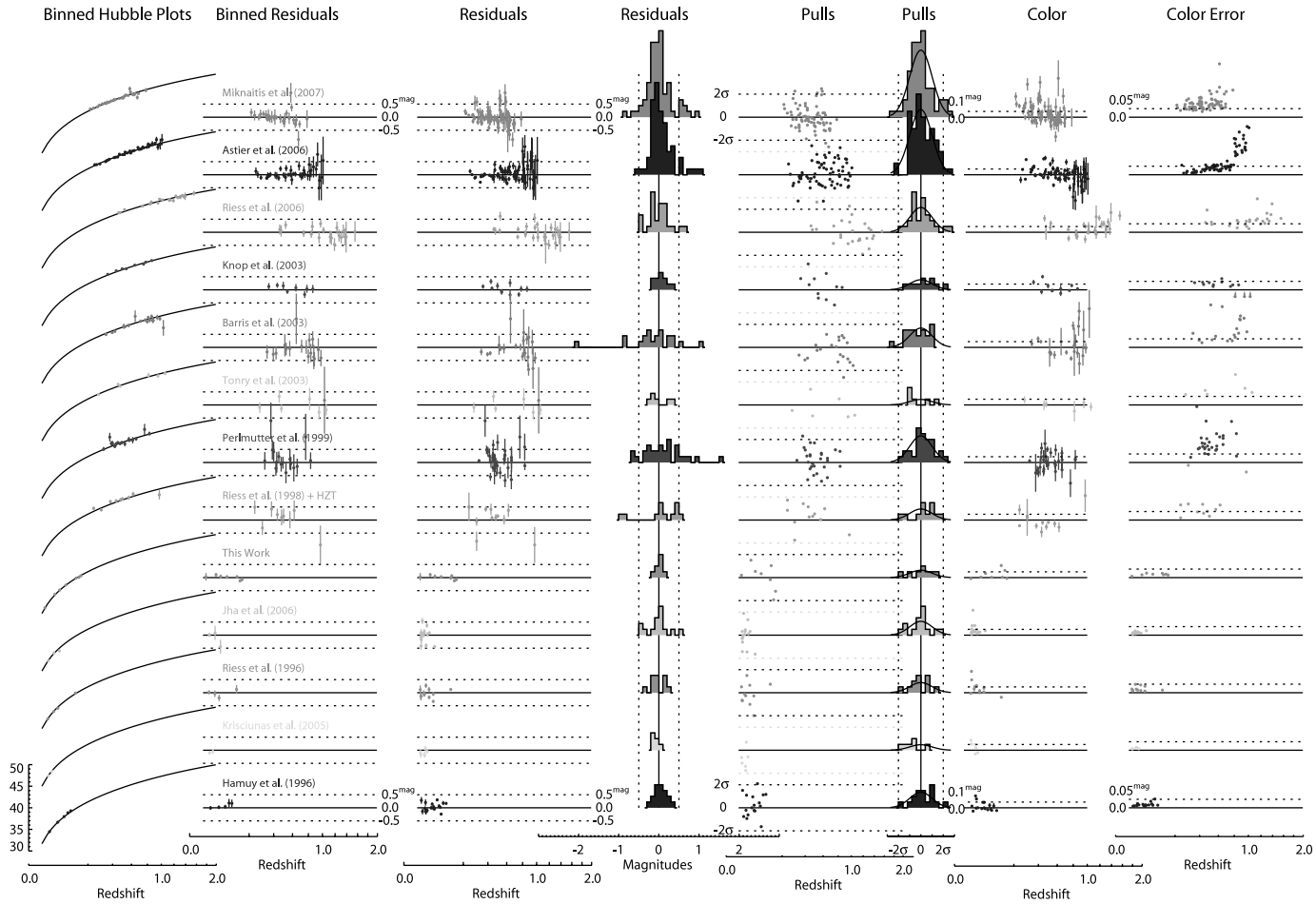

FIG. 8.—From left to right: (*a*) Hubble diagrams for the various samples; (*b*) binned magnitude residuals from the best fit (bin width: $\Delta z = 0.01$); (*c*) unbinned magnitude residuals from the best fit; (*d*) histogram of the residuals from the best fit; (*e*) pull of individual SNe as a function of redshift; (*f*) histogram of pulls; (*g*) SN color as a function of redshift; (*h*) uncertainty of the color measurement as an illustration of the photometric quality of the data. [*See the electronic edition of the Journal for a color version of this figure.*]

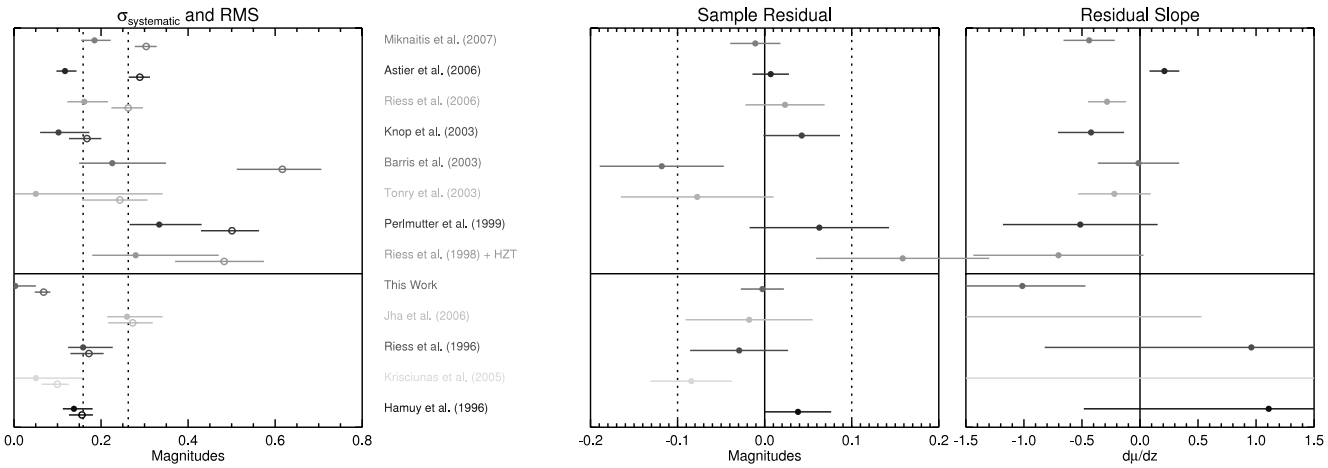

FIG. 9.—From left to right: Systematic dispersion (*filled circles*) and rms around the best-fit model (*open circles*); the mean, sample averaged, deviation from the best-fit model; the slope of the Hubble residual (in magnitudes) vs. redshift, $d\mu_{\rm residual}/dz$. The parameters characterizing the different samples are used to uncover potential systematic problems. [*See the electronic edition of the Journal for a color version of this figure.*]

Figure 9 shows diagnostic variables used to test for consistency between the various samples. The leftmost plot shows the systematic dispersion and rms around the best-fit model. One expects that there is an intrinsic dispersion associated with all SNe that provides a lower limit to the sample-dependent systematic dispersion. To estimate the intrinsic dispersion one can look at various quantities, such as the smallest $\sigma_{\rm sys}$ or, perhaps more appropriately, the median of $\sigma_{\rm sys}$. The median of $\sigma_{\rm sys}$, which is about 0.15 mag (shown as the leftmost dashed vertical line), is a robust measure of the intrinsic dispersion, as long as the majority of samples are not dominated by observer-dependent, unaccounted-for uncertainties.

As a test for tension between the data sets, we compare for each sample the average residual from the best-fit cosmology. This is shown in the middle panel of Figure 9. As can be seen, most samples fall within 1 σ, and none deviate by more then 2 σ. The larger samples show no indication of inconsistency. This changes if one considers, instead of the mean, the slope, $d\mu_{\rm residual}/dz$, of the residuals as a function of the redshift. The right panel of Figure 9 shows a large fraction of significant outliers in the slope. The largest slope outlier is found for the Miknaitis et al. (2007) sample (see also the middle panel of Fig. 8). The sign of the slope is consistent with the presence of a Malmquist bias (see Wood-Vasey et al. 2007 for a discussion). The uncertainties associated with such a Malmquist bias are discussed in § 5.5. While in general there is no clear trend in the sign of the slope deviations, it is clear that any results that depend on the detailed slope, such as a changing equation of state, should be treated with caution.

5. SYSTEMATIC ERRORS

Detailed studies of the systematic effects have been published as part of the analysis of individual data sets. The list includes photometric zero points, Vega spectrum, light curve fitting, contamination, evolution, Malmquist bias, *K*-corrections, and gravitational lensing, which have also been discussed in earlier work by authors of this paper (Perlmutter et al. 1997, 1999; Knop et al. 2003; Astier et al. 2006; Ruiz-Lapuente 2007; Wood-Vasey et al. 2007).

Some sources of systematic errors are common to all surveys and will be specifically addressed for the full sample. Other sources of systematic errors are controlled by the individual observers. The degree with which this has been done for the various data samples entering the analysis is very different. The SNLS—which is using a single telescope and instrument for the search and follow-up and which has detailed multiband photometry for nearly all its SNe—has a strong handle on a subset of the observation-dependent systematics uncertainties. With the exception of the ESSENCE SN data sample, other high-redshift samples are smaller and will contribute less to the final results.

We handle the two types of systematic errors separately: systematic errors that can be associated with a sample (e.g., due to observational effects) and those that are common to all the samples (e.g., due to astrophysical or fundamental calibration effects). To first order, the measurement of cosmological parameters depends on the relative brightness of nearby SNe ($z \sim 0.05$) compared to their high-redshift counterparts ($z \sim 0.5$). If low- and high-redshift SNe are different, this can be absorbed in different absolute magnitudes *M*. We hence cast the common systematic uncertainties into an uncertainty in the difference $\Delta M = M_{\rm low} - M_{\rm high\text{-}z}$. We have chosen $z_{\rm div} = 0.2$ as the dividing redshift as it conveniently splits the samples according nearby and distant SN searches. Note, however, that our resulting systematic errors change by less than 25% of its value for $z_{\rm div}$ in the range 0.1–0.5. In addition we allow for a set of extra parameters, ΔM_i, one for each sample *i*.

Systematic uncertainties are then propagated by adding these nuisance parameters to μ_B:

$$\mu_B' = \begin{cases} \mu_B + \Delta M_i & \text{for } z_{\rm div} < 0.2, \\ \mu_B + \Delta M_i + \Delta M & \text{for } z_{\rm div} \geq 0.2, \end{cases} \quad (5)$$

with the term $\Delta M^2/\sigma^2_{\Delta M} + \sum_{i=1}^{N_{\rm samples}} \Delta M_i^2/\sigma^2_{\Delta M_i}$ being added to the χ^2 as defined through equation (3).

We have checked that this treatment of systematic errors is consistent (in our case to better than 5% of its value) with the more common procedure, applicable to one-dimensional constraints, in which part of the input data are offset by $\pm\sigma_{\Delta M}$ to obtain the systematic variations in the resulting parameter (e.g., *w* or Ω_M).

In the following we discuss the different contributions to $\sigma_{\Delta M}$, and summarize them in § 5.9. The resulting systematic errors on the cosmological parameters are discussed in § 6.

5.1. *Stretch and Evolution*

With the large statistics at hand one can test the errors associated with the empirical stretch and color corrections. These corrections would become sources of systematic error if (1) different SN populations were to require different corrections and (2) if the SN

TABLE 4
Fit Parameters as Obtained for Different Supernova Subsamples

Subset	N_{SN}	α	β	Ω_M[a]	w[b]
All	307	1.24 (0.10)	2.28 (0.11)	0.29 (0.03)	−0.97 (0.06)
$z > 0.2$.....	250	1.46 (0.16)	2.26 (0.14)	...	...
$z \leq 0.2$.....	57	1.07 (0.12)	2.23 (0.21)	...	...
$s < 0.96$.....	155	1.56 (0.27)	2.18 (0.18)	0.27 (0.05)	−0.98 (0.09)
$s \geq 0.96$.....	152	1.51 (0.37)	2.34 (0.17)	0.30 (0.04)	−0.93 (0.07)

[a] A flat universe was assumed in the constraints on Ω_M.
[b] Constraints on w were obtained from combining SNe with CMB and BAO measurements. A flat universe was also assumed. (see § 6 for more details).

populations were to show differences between nearby and distant objects (either due to selection effects or due to evolution of the SN environment).

A potential redshift dependence of the correction parameters can be tested by separately fitting low-redshift and high-redshift objects. For this test, a ΛCDM cosmology was assumed with $\Omega_M = 0.28$ and $\Omega_M = 0.72$ (the values we obtain from the fit of the full sample); however, the results are rather insensitive to the assumed cosmological parameters. The obtained fitted parameters α and β are presented in Table 4.

The values of β at high and low redshift agree very well, providing strong constraints on evolution of the color-correction. Such evolution effects could arise, for example, due to a different mix of dust reddening and intrinsic color at different redshifts. The fact that β agrees so well supports the choice of the empirical color correction.[43]

The α at low redshift and high redshift are only marginally consistent with each other. We will take the difference at face value and estimate the impact it would have on the final result. The average stretch is $\langle s \rangle \approx 0.96$ and hence the difference in the average stretch correction is $\langle 1 - s \rangle \Delta\alpha \approx 0.015$. If α indeed is redshift-dependent and this was not accounted for, one would obtain a bias of $\Delta M = 0.015$ mag.

Effects of potentially different SN populations should be considered as well. It has recently been argued by Scannapieco & Bildsten (2005) and Mannucci et al. (2006) that one needs to allow for two types of SN-progenitor timescales to explain the observed rates in different galaxy types. One class of objects traces the star formation rate directly, while the second class has a delay time trailing the star formation rate by a few billion years. If indeed two populations are present, they might evolve differently with redshift. It is therefore important to check that the empirical corrections suit both populations. To test the effect of different SN populations one can subdivide the sample according to SN subtypes or host environments (Sullivan et al. 2003; Howell et al. 2007).

Sullivan et al. (2006) have found using well-observed SNe and hosts from SNLS that the stretch of a light curve is correlated with its host environment as well as with the two classes of SN-progenitor systems postulated by Scannapieco & Bildsten (2005) and Mannucci et al. (2006). Therefore, we divide the SN sample into two approximate equally large samples with $s < 0.96$ and $s \geq 0.96$. The two independent samples are then fitted, with the results shown in Table 4. The resulting parameters Ω_M (for a flat universe) and w (for a flat universe together with BAO+CMB) for the two samples are less than 1 σ apart, and hence, there is no evidence for an underlying systematic effect. Nevertheless, this will be a very important number to watch, once future high-quality SN data sets are added. (Note that, while the resulting values of αs for the two samples are consistent with each other, they appear inconsistent with the value obtained for the complete sample. This apparent inconsistency arises in part due to a bias introduced by dividing the stretch distribution in the middle. Larger stretch SNe, misclassified due to measurement errors as belonging to the low-stretch SNe sample, as well as lower stretch SNe, misclassified as belonging to the large stretch SNe sample, will for both samples result in a α biased to larger values.)

We have also investigated whether the sample can be subdivided according to the color of the SNe. We found that the results of such a test can be very misleading. While in principle one would expect to find that the best-fitted cosmological parameters do not depend on color selection criteria (e.g., $c < c_{\rm cut}$ and $c > c_{\rm cut}$), we find by means of Monte Carlo simulation described in § 4.2 that a significant bias is introduced into the measurements. This bias is also observed in the data. For example, by choosing $c_{\rm cut} = 0.02$ we find that for our sample of SNe Ω_M changes by ± 0.1. The bias arises from truncating an asymmetric distribution. In the case of color, the asymmetry in the distribution is introduced by the fact that extinction by dust leads only to reddening. Hence, the number of objects that would belong to $c_{\rm true} < c_{\rm cut}$ but, due to a large measurement error, are fitted with $c_{\rm observed} > c_{\rm cut}$, are not compensated by objects misclassified in the opposite way. The number of misclassified objects is a function of the measurement errors and, hence, is larger toward higher redshift. The simulated data sets result in a significant bias both in Ω_M as well as β. The size of the bias, however, depends on assumptions made for the underlying color distribution. Hence, for the current data sample, splitting the data set in two color bins introduces a bias so large and difficult to control that the results of the test become meaningless. Note that if one had very small error bars on the color measurement over the full redshift range (as obtained from a dedicated space-based survey [Aldering 2005]), the bias can be kept small. This would allow for additional tests of systematic uncertainties due to reddening corrections.

5.2. *Sample Contamination*

As discussed in § 4.3, the method of robust statistics was applied to limit the effect of outliers, which could be present if the data are contaminated by non–Type Ia SNe, or by other events that do not have the standard candle properties of regular SN Ia. It was shown in § 4.3 that the bias due to contamination can be limited for this analysis to $\Delta M = 0.015$ mag, which we hence use as the uncertainty due to contamination.

In previous compilations, such as that of Riess et al. (2004, 2007) no formal outlier criteria were applied. Instead, with some exceptions, the original classifications made by the authors of the data sample were used. Spurious candidates are sometimes removed from the data samples by hand (see, e.g., Astier et al. 2006), making it extremely difficult to estimate the effect of the remaining contamination. Our method of outlier rejection provides a simple and objective alternative.

5.3. *Light Curve Model and K-Corrections*

The light curve model (Guy et al. 2005) is a parametric description with two free parameters. As such, it has limitations in capturing the full diversity of Type Ia SNe. By visual inspection we find, for example, that the fitted maximum magnitude can differ from the data by a few hundredths of a magnitude. A particular problem could arise if the observation strategies for nearby and distant SNe differ. In fact, the high-redshift data sets have on

[43] Note that if β were not obtained by fitting but instead was fixed, e.g., $\beta = R_B = 4.1$, a bias can be expected (and might have already been observed, see Conley et al. 2007) if the average reddening changes as a function of redshift.

average earlier observations of the light curve, which is a result of the rolling-search techniques frequently used to find and follow-up SNe. Hence, when comparing low-z to high-z SNe, the fitted light curve parameters are obtained from slightly different parts of the light curve. The mismatch between template and the data light curve might thus be more pronounced in one sample than the other. To quantify the effect, we have performed an extensive Monte Carlo simulation. A set of *BVR* light curve templates are obtained from a quartic spline fit to data, including the well-observed SNe 1990N, 1994D, 1998aq, 2001el, 2002bo, 2003du, 2004eo, and 2005cf (Strovink 2007). The templates are then used to sample random realizations of the light curves with cadence, S/N, and date of the first detection of the nearby and distant SN sample. These simulated light curves are then fitted. The difference in the stretch and color-corrected peak magnitude between the nearby and distant sample can be used to estimate the systematic uncertainty. For the nine templates we obtain the average difference between nearby and distant SNe of -0.02 mag with an rms scatter of 0.015. We adopt an associated systematic uncertainty of $\Delta M = 0.02$ mag due to this.

There is another source of uncertainty arising from the diversity of SNe Ia light curves. If a certain class of SNe is misrepresented (e.g., if they are brighter than average for their typically fitted stretch value) and if the fraction of such SNe changes as a function of redshift, it will lead to a systematic bias in the cosmological parameters. Appendix D has addressed this issue by subdividing the sample according to stretch and redshift. If a significant light curve misrepresentation were present, one would expect to see differences in the fitted light curve – correction parameters. No statistically significant differences have been observed, and we assign no additional contribution to the uncertainties from such an effect.

The light curve model is based on a spectral template series. It thereby eliminates the need for a separate K-correction (see § 3.3). The model has been trained with nearby SNe data and hence will be affected by systematic errors associated with that training data. These are largest for the U band, which suffers from low training statistics and difficult flux calibration. However, the validity of the model in the U band has been verified with the SNLS data set to better than 0.02 mag (Astier et al. 2006). Here we adopt their assessment of the resulting systematic error of $\Delta M = 0.02$.

5.4. *Photometric Zero Points*

With present methods, ground-based photometric zero-point calibration is generally limited to an accuracy of $\gtrsim 1\%$ (Stubbs & Tonry 2006). The largest contribution to the photometric error of the peak magnitude arises from the color correction $\Delta M \sim \beta \Delta c$. The color measurement is based on the measurement of the relative flux in two (or more) bands and as a result some of the uncertainties cancel. Nevertheless, since the color of SNe at different redshifts are obtained from different spectral regions, the uncertainty in the reference Vega spectrum limits the achievable accuracy to $\Delta c \approx 0.01$–0.015 mag (Stritzinger et al. 2005; Bohlin & Gilliland 2004).

Here we assume an uncertainty of $\Delta M = 0.03$ for the photometric peak magnitude due to zero-point calibration. Part of this uncertainty is common to all samples (as the same set of calibration stars is being used), while the other part is sample-dependent (e.g., tied to the calibration procedure), and we divide the error equally among the two categories.

5.5. *Malmquist Bias*

Malmquist bias arises in flux-limited surveys, when SNe are detected because they are overly bright. What matters for cosmology is whether the bias is different for the low-z and high-z samples. Perlmutter et al. (1999), Knop et al. (2003), and Astier et al. (2006) have evaluated the effects of Malmquist bias for the SCP and SNLS SN samples as well as the nearby SN sample and found that they nearly cancel. Since an individual estimate of Malmquist bias for all the different samples is beyond the scope of this work, we attribute a conservative systematic uncertainty of $\Delta M = 0.02$ (Astier et al. 2006) for all samples, which is consistent with previous estimates.

In addition, we investigated whether the significant redshift dependence of the Hubble residuals observed for the Miknaitis et al. (2007) sample (see § 4.4), if interpreted as due to Malmquist bias, exceeds our claimed uncertainty. A simulation was performed in which we introduced a magnitude cutoff such that the resulting slope, $d\mu/dz$, matches the observed slope of -0.6. The associated Malmquist bias with that sample is then ~ 0.05 mag. If this is compared to the average Malmquist bias obtained for magnitude-limited searches, the extra bias is only 0.03 mag larger—not much larger than the systematic uncertainty we have adopted. While we do not treat the ESSENCE data sample differently from the others, we note that Wood-Vasey et al. (2007) made their extinction prior redshift-dependent to account for the fact that at higher redshifts an increasingly larger fraction of the reddened SNe was not detected. The linear color correction employed in our analysis is independent of a prior and therefore unaffected by a redshift-dependent reddening distribution.

5.6. *Gravitational Lensing*

Gravitational lensing decreases the mode of the brightness distribution and causes increased dispersion in the Hubble diagram at high redshift (see Fig. 10). The effect has been discussed in detail in the literature (Sasaki 1987; Linder 1988; Bergström et al. 2000; Holz & Linder 2005). We treat lensing as a statistical phenomenon only, although with the detailed optical and NIR data available for the GOODS field, the mass distribution in the line of sight and hence the lensing (de)magnification may be estimated for individual SNe (Jönsson et al. 2006). What is important for this work is that they find no evidence for selection effects (i.e., Malmquist bias) due to lensing of the high-redshift SNe.

Considering both strong and weak lensing, Holz & Linder (2005) found that lensing will add a dispersion of $0.093z$ mag, which, if the statistics of SNe is large enough, can be approximated as an additional Gaussian error. Here we added the additional dispersion from gravitational lensing in quadrature to the "constant" systematic dispersion and observational error. This effectively deweights the high-redshift SNe. However, only for the highest-redshift SNe is the additional uncertainty comparable to that of the intrinsic dispersion.

Flux magnification and demagnification effects due to over- or underdensities of matter near the line of sight cancel. But one obtains a bias if magnitudes instead of fluxes are used. However, the bias is $0.004z$ mag and therefore still much smaller than the statistical error on the luminosity distance obtained from the ensemble of high-redshift SNe. While not yet relevant for this analysis, future high-statistics samples will have to take this effect into account.

Another potential bias is introduced by the $3\,\sigma$ outlier rejection, since the lensing PDF is asymmetric. Using the PDFs of Holz & Linder (2005) we have checked that the bias is never larger than $0.006z$ mag. We take the worst-case value of 0.009 mag (i.e., for a SNe at $z \approx 1.5$) as a conservative systematic uncertainty for gravitational lensing, since this is still an almost negligible value.

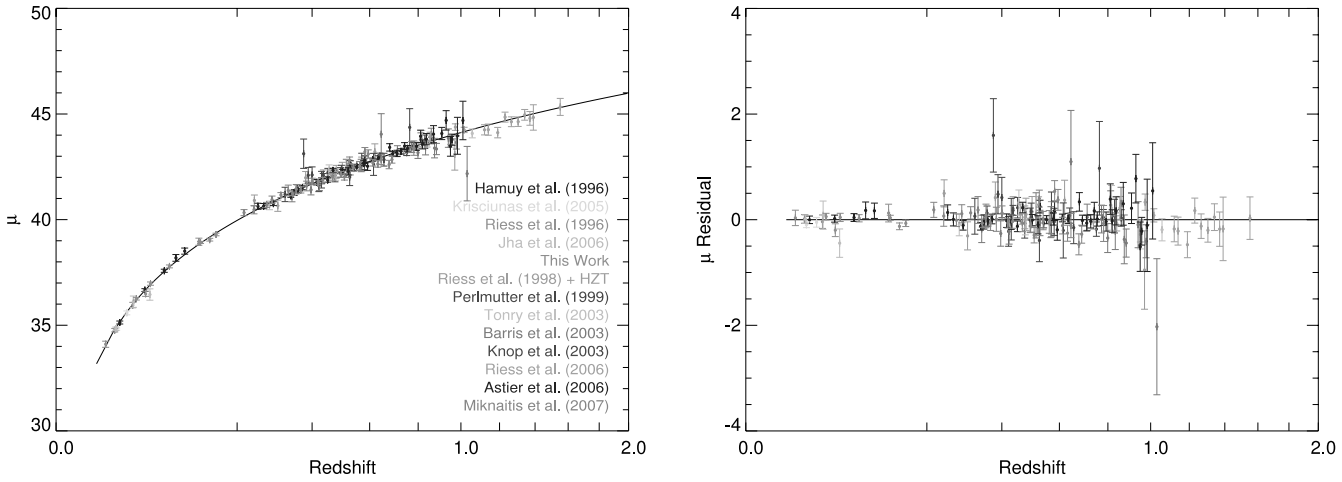

FIG. 10.—*Top*: Binned Hubble diagram (bin size $\Delta z = 0.01$). *Bottom*: Binned residuals from the best-fitting cosmology. [*See the electronic edition of the Journal for a color version of this figure.*]

5.7. *Gray Intergalactic Dust*

The possibility that SNe are dimmed due to hypothetical gray intergalactic dust, as suggested by Aguirre (1999), was constrained by Östman & Mörtsell (2005) and Mörtsell & Goobar (2003) by studying the colors of high-redshift quasars. Applying their constraints on intergalactic dust, we find that the cosmological parameters are shifted by about 1 statistical standard deviation, i.e., for a flat universe $\Delta\Omega_M = -0.03$. This should not be considered a systematic uncertainty, but rather an upper limit on the effect of hypothetical large grains of cosmic dust in the line of sight.

5.8. *Galactic Extinction*

All light curve data were corrected for Galactic extinction using the extinction law of Cardelli et al. (1989) using an R_V of 3.1. The $E(B-V)$ values were derived from the sky map of Schlegel et al. (1998) and have a typical statistical error of 10%. For nearby SNe we hence obtain an additional uncertainty of

$$\Delta\mu_B \approx (R_B - \beta)\sigma(E(B-V)) \approx 0.2E(B-V), \qquad (6)$$

where β is the color correction coefficient from equation (2). We add this statistical error in quadrature to each nearby SNe. High-redshift SNe are measured in redder bands and, since $R_R \approx \beta$, are less affected by Galactic extinction.

There is also a common systematic error of 10% in the overall reddening normalization. The average Galactic $E(B-V)$ for the low-redshift sample is 0.063, and we add a $0.063 \times 0.2 = 0.013$ mag systematic uncertainty to ΔM.

5.9. *Summary of Systematic Errors*

In our treatment of the above systematic errors we distinguish between systematic errors common between data sets, which are largely of astrophysical nature, and the more observer-dependent ones associated with individual samples. Table 5 summarizes what are considered the relevant contributions to the systematic uncertainties in this analysis. They are propagated into the final result through equation (5).

6. COSMOLOGICAL FIT RESULTS

Our analysis of cosmological model fits includes both statistical and systematic errors. The individual contributions to the systematic error identified in Table 5 are of very different nature and hence are assumed uncorrelated. We hence obtain the combined systematic error by adding in quadrature the individual contributions. The resulting error was propagated according to the prescription described in § 5. Our constraints on the matter density Ω_M, assuming a flat universe, are summarized in Table 6. Both statistical (68% confidence) and systematic errors are quoted.

Figure 11 plots our results for the joint fit to the matter density and cosmological constant energy density, Ω_M and Ω_Λ, and the effect of varying the outlier cut, while Figure 12 illustrates the effects of systematics. For comparison with previous work, Figure 13 shows our joint constraints on Ω_M and Ω_Λ (statistical error only) and the Riess et al. (2007) constraints obtained from the Gold compilation of data primarily from the HZT, SCP, and SNLS (Riess et al. 2007) and a recent compilation of Davis et al. (2007), which is based on light curve fits from Riess et al. (2007) and Wood-Vasey et al. (2007). The results obtained in this work are consistent with those of previous studies; however, compared to the recent SN fit results of Astier et al. (2006), Riess et al. (2007), Wood-Vasey et al. (2007), and Davis et al. (2007), we obtain a 15%–30% reduction in the statistical error.

About half the improvement can be attributed to the new SCP Nearby 1999 SNe. Their impact is evident in the rightmost column of Figure 13 (as well as in Fig. 14). The impact of these SNe is somewhat larger because the sample has a best-fit systematic uncertainty of zero. If instead one would introduce the requirement that $\sigma_{\rm sys} \geq 0.1$, there would be an increase of about 10% in the uncertainties of the cosmological parameters.

Figure 13 shows the constraints on the equation of state parameter w (assumed constant) and Ω_M. A flat universe was assumed. Again, the constraints are consistent with, but stronger

TABLE 5
MOST RELEVANT COMMON AND SAMPLE-DEPENDENT SYSTEMATIC ERRORS OF THIS ANALYSIS

Source	Common (mag)	Sample-dependent (mag)
α and β correction	0.015	...
Contamination	...	0.015
Light curve model	0.028	...
Zero point	0.021	0.021
Malmquist bias	...	0.020
Gravitational lensing	...	0.009*
Galactic extinction normalization	0.013	...
Total in mag	$\Delta M = 0.040$	$\Delta M_i = 0.033$

TABLE 6
FIT RESULTS ON COSMOLOGICAL PARAMETERS Ω_M, Ω_k, AND w

Fit	Ω_M	Ω_k	w
SNe	$0.287^{+0.029+0.039}_{-0.027-0.036}$	0 (fixed)	-1 (fixed)
SNe + BAO	$0.285^{+0.020+0.011}_{-0.020-0.009}$	0 (fixed)	$-1.011^{+0.076+0.083}_{-0.082-0.087}$
SNe + CMB	$0.265^{+0.022+0.018}_{-0.021-0.016}$	0 (fixed)	$-0.955^{+0.060+0.059}_{-0.066-0.060}$
SNe + BAO + CMB	$0.274^{+0.016+0.013}_{-0.016-0.012}$	0 (fixed)	$-0.969^{+0.059+0.063}_{-0.063-0.066}$
SNe + BAO + CMB	$0.285^{+0.020+0.011}_{-0.019-0.011}$	$-0.009^{+0.009+0.002}_{-0.010-0.003}$	-1 (fixed)
SNe + BAO + CMB	$0.285^{+0.020+0.010}_{-0.020-0.010}$	$-0.010^{+0.010+0.006}_{-0.011-0.004}$	$-1.001^{+0.069+0.080}_{-0.073-0.082}$

NOTES.—The parameter values are followed by their statistical ($\sigma_{\rm stat}$) and systematic ($\sigma_{\rm sys}$) uncertainties. The parameter values and their statistical errors were obtained from minimizing the χ^2 of eq. (3). The fit to the SNe data alone results in a χ^2 of 310.8 for 303 degrees of freedom with a $\Delta\chi^2$ of less than one for the other fits. The systematic errors were obtained from fitting with extra nuisance parameters according eq. (5) and subtracting from the resulting error, $\sigma_{\rm w/sys}$, the statistical error: $\sigma_{\rm sys} = (\sigma^2_{\rm w/sys} - \sigma^2_{\rm stat})^{1/2}$.

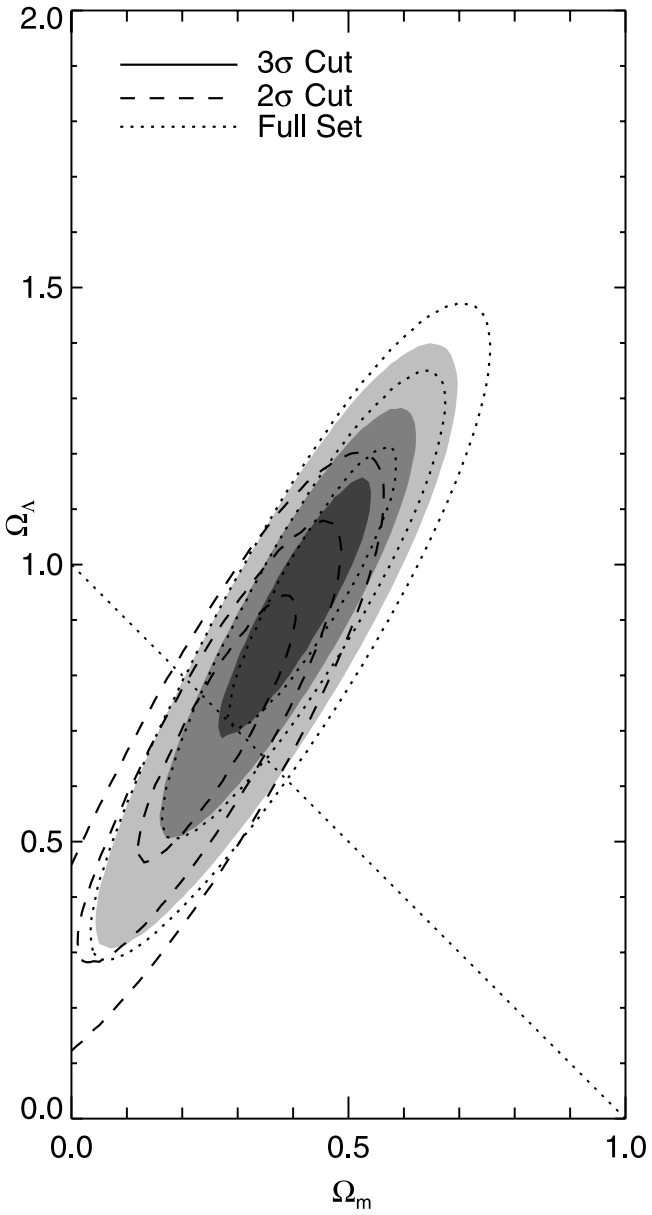

FIG. 11.—Contours at 68.3%, 95.4%, and 99.7% confidence level on Ω_Λ and Ω_M plane from the Union SNe set. The result from the robustified set, obtained with a $\sigma_{\rm cut} = 3$ outlier cut, is shown as filled contours. The empty contours are obtained with the full data set (*dotted line*) and $\sigma_{\rm cut} = 2$ outlier rejected data set (*dashed line*). As can be seen, outlier rejection shifts the contours along the degenerate axis by as much as 0.5 σ toward a flat universe. In the remaining figures, we refer to the $\sigma_{\rm cut} = 3$ outlier rejected set as the Union set.

than, those from Riess et al. (2007) and Davis et al. (2007). The current SN data do not provide strong constraints on the equation of state parameter w by itself, since it is to a large extent degenerate with Ω_M. However, the degeneracy can be broken by combining with other measurements involving Ω_M. Figure 14 shows the constraints obtained from the detection of baryon acoustic oscillations (BAOs; Eisenstein et al. 2005) and from the 5 year data release of the *Wilkinson Microwave Anisotropy Probe* (CMB; Dunkley et al. 2008). The constraints from the CMB data follow from the reduced distance to the surface of last scattering at $z = 1089$ (or shift parameter). It is important to realize that for parameter values far from the concordance model, the shift in the sound horizon must also be taken into account. The reduced distance R is often written as

$$R_{\rm conc} = (\Omega_M H_0^2)^{1/2} \int_0^{1089} dz/H(z), \tag{7}$$

where the Hubble parameter is $H(z) = H_0[\Omega_M(1+z)^3 + (1-\Omega_M)(1+z)^{3(1+w)}]^{1/2}$. The *WMAP* 5 year CMB data alone yield $R_0 = 1.715 \pm 0.021$ for a fit assuming a constant w (Komatsu et al. 2008; *WMAP* Web site[44]). Defining the corresponding χ^2 as $\chi^2 = [(R_{\rm conc} - R_0)/\sigma_{R_0}]^2$, one can then deduce constraints on Ω_M and w. However, this assumes a standard matter (and radiation) dominated epoch for calculating the sound horizon. The more proper expression for the shift parameter accounts for deviation in the sound horizon:

$$R = (\Omega_M H_0^2)^{1/2} \int_0^{1089} dz/H(z) \times \left[\int_{1089}^{\infty} dz/\sqrt{\Omega_M(1+z)^3} \Big/ \int_{1089}^{\infty} dz/(H(z)/H_0) \right]. \tag{8}$$

Since dark energy is generally negligible at high redshift, the factor in square brackets is usually unity [for example, it deviates from unity by less than 1% even for $w_0 = -1$, $w_a = 0.9$, i.e., $w(z = 1089) = -0.1$]. However, for extreme models that upset the matter-dominated behavior at high redshifts, the correction will be important in calculating whether the geometric shift parameter accords with CMB observations (apart from any issue of fitting other observations). Violation of early matter domination causes the "wall" in likelihood apparent in Figure 16. Also see, e.g., Linder & Miquel (2004) and Wright (2007).

[44] *WMAP* Web site. 2008, http://lambda.gsfc.nasa.gov/product/map/dr3/params/wcdm_sz_lens_wmap5.cfm.

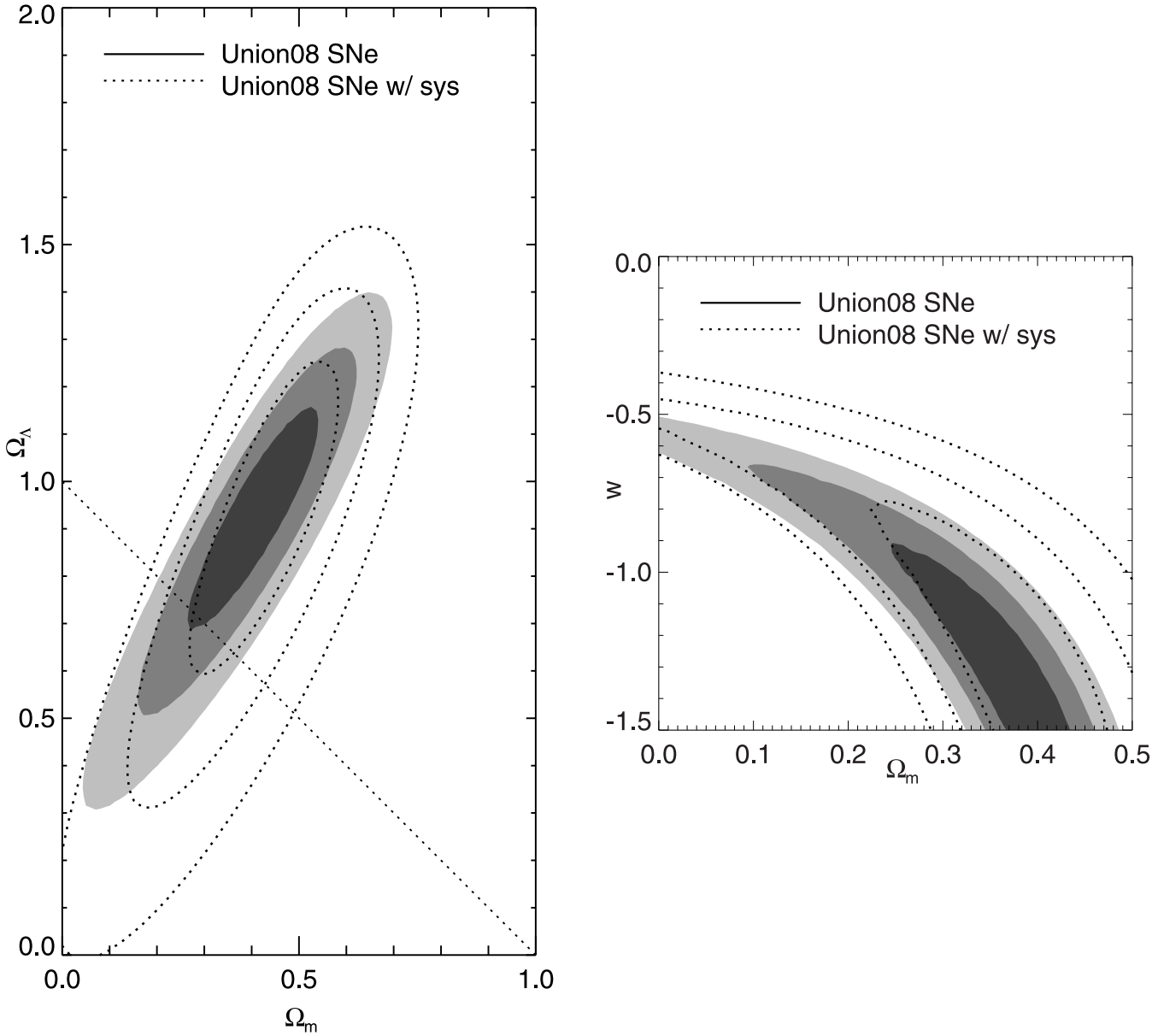

FIG. 12.—*Left plot*: Contours at 68.3%, 95.4%, and 99.7% confidence level on Ω_Λ and Ω_M obtained with the Union set, without (*filled contours*) and with (*open contours*) inclusion of systematic errors. The right plot shows the corresponding confidence level contours on the equation of state parameter w and Ω_M, assuming a constant w.

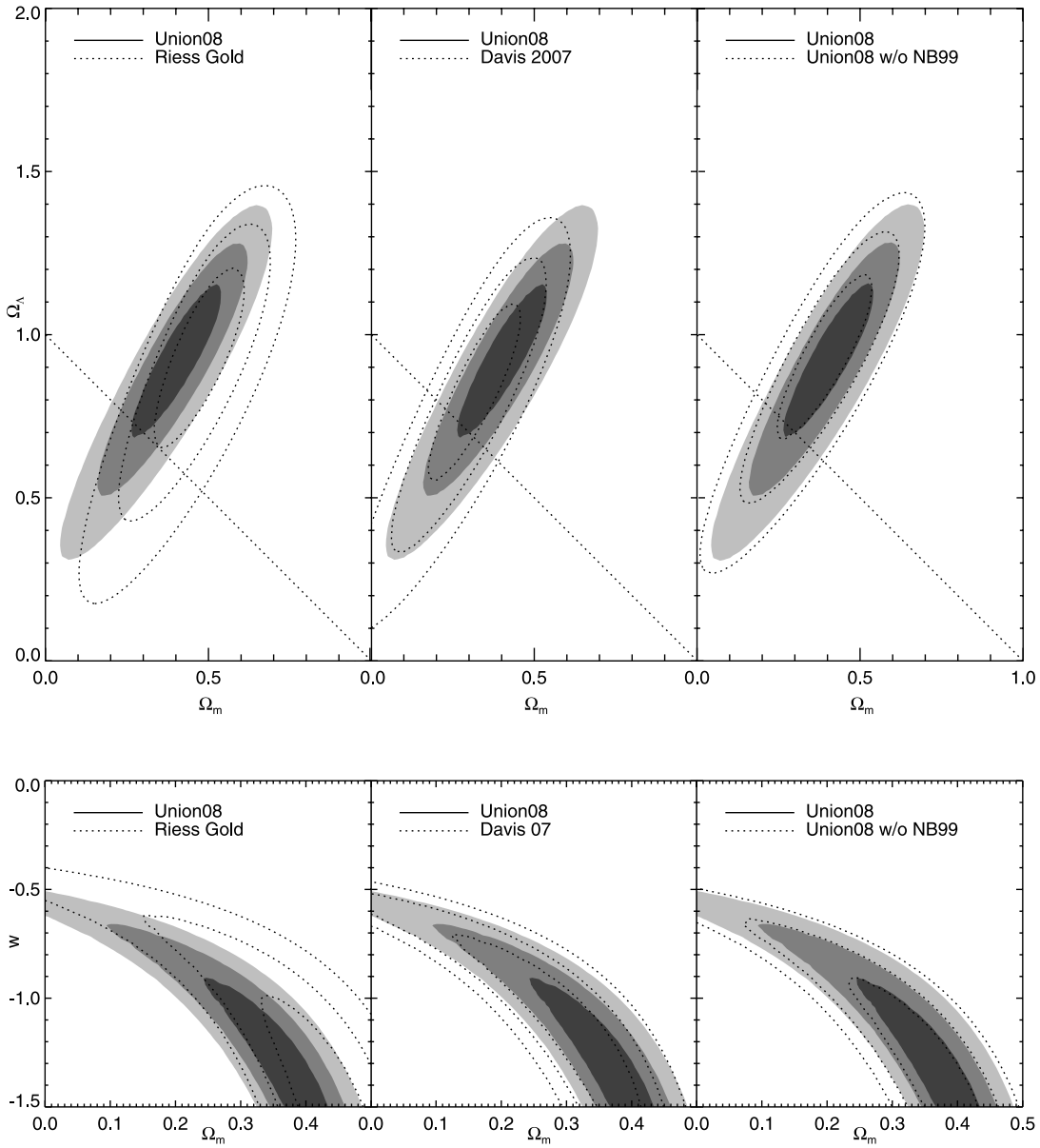

FIG. 13.—Contours at 68.3%, 95.4%, and 99.7% confidence level on Ω_Λ and Ω_M (*top row*) and Ω_M and w (*bottom row*). The results from the Union set are shown as filled contours. The empty contours in the left column represent the Gold sample (Riess et al. 2004, 2007), and the middle column the constraints from Davis et al. (2007). While our results are statistically consistent with the previous work, the improvements in the constraints on the cosmological parameters are evident. The right column shows the impact of the SCP Nearby 1999 data.

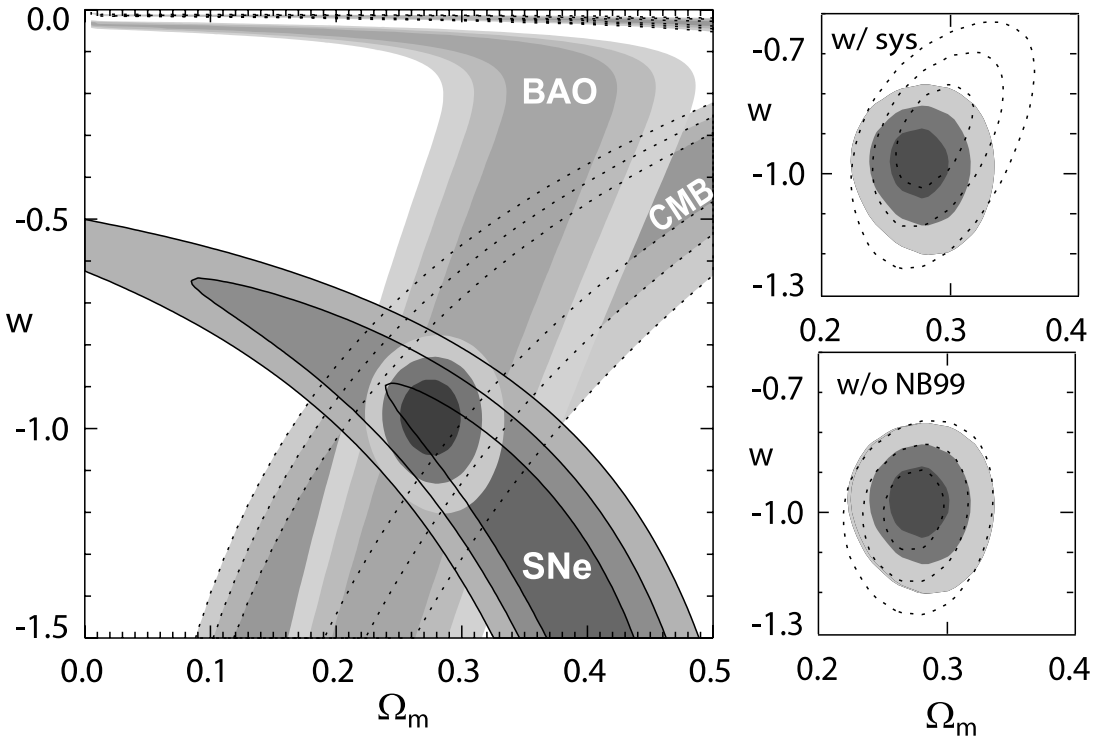

FIG. 14.—Contours at 68.3%, 95.4%, and 99.7% confidence level on w and Ω_M, for a flat universe. The top plot shows the individual constraints from CMB, BAO, and the Union SN set, as well as the combined constraints (*filled gray contours*, statistical errors only). The upper right plot shows the effect of including systematic errors. The lower right plot illustrates the impact of the SCP Nearby 1999 data. [*See the electronic edition of the Journal for a color version of this figure.*]

BAO measurements from the SDSS data (Eisenstein et al. 2005) provide a distance constraint at a redshift $z = 0.35$. Percival et al. (2007) have derived BAO distances for $z = 0.2$, in addition to the $z = 035$ SDSS-data point, using the combined data from SDSS and 2dFGRS. However, some points of tension were noted between the data sets (Percival et al. 2007; see also Sánchez & Cole 2008), especially evident for ΛCDM models. We confirm this observation and found that the $z = 0.2$ data point, if combined with SN and CMB data according to the prescription in Appendix A of Percival et al. (2007) leads to an 2.5 σ inconsistency. Neither the $z = 0.35$ BAO data point from Percival et al. (2007) nor the slightly weaker constraint from Eisenstein et al. (2005) shows such kind of tension. Given the differences between the two data sets, we use the $z = 0.35$ SDSS data point of Eisenstein et al. (2005) but with the caveat that BAO constraints need further clarification. Eisenstein et al. (2005) provides a constraint on the distance parameter A:

$$A(z) = (\Omega_M H_0^2)^{1/2} H(z)^{-1/3} z^{-2/3} \left[\int_0^z dz'/H(z') \right]^{2/3} \times \left[\int_{1089}^{\infty} dz/\sqrt{\Omega_M (1+z)^3} \Big/ \int_{1089}^{\infty} dz/(H(z)/H_0) \right], \quad (9)$$

to be $A(z = 0.35) = 0.469 \pm 0.017$. Note that BAOs also depend on accurate accounting of the sound horizon and receive the same correction factor shown in brackets in equation (8). This results in a similar wall to the acceptable confidence contour reflecting violation of early matter domination. To see that such violation has severe implications, note that most models above the wall have a total linear growth factor a factor of 10 below the concordance cosmology.

The joint constraints from SN data, BAO, and CMB are shown in Figure 14, and the corresponding numbers are given in Table 6. As can be seen, the constraints obtained from combining either BAO or CMB with SNe data give consistent results and comparable error bars, while the combination of all three measurements improves only the statistical error. The impact of including systematic errors (only from SNe, from eq. [5]) is shown in the upper right panel of Figure 14.

The results quoted so far were derived assuming a flat universe. Allowing for spatial curvature Ω_k, our constraints from combining SNe, CMB and BAO are consistent with a flat ΛCDM universe (as seen in Table 6). Figure 15 shows the corresponding constraints in the Ω_M-Ω_Λ plane.

Finally, one can attempt to investigate constraints on a redshift-dependent equation of state (EOS) parameter $w(z)$. Initially, we consider this in terms of

$$w(z) = w_0 + w_a \frac{z}{1+z}, \quad (10)$$

shown by Linder (2003) to provide excellent approximation to a wide variety of scalar field and other dark energy models. Later, we examine other aspects of time variation of the dark energy EOS. Assuming a flat universe and combining the Union set with constraints from CMB, we obtain constraints on w_0, the present value of the EOS, and w_a, giving a measure of its time variation, as shown in Figure 16. (A cosmological constant has $w_0 = -1$, $w_a = 0$.) Due to degeneracies within the EOS and between the EOS and the matter density Ω_M, the SN data set alone does not give appreciable leverage on the dark energy properties. By adding other measurements, the degeneracies can be broken and currently modest cosmology constraints obtained.

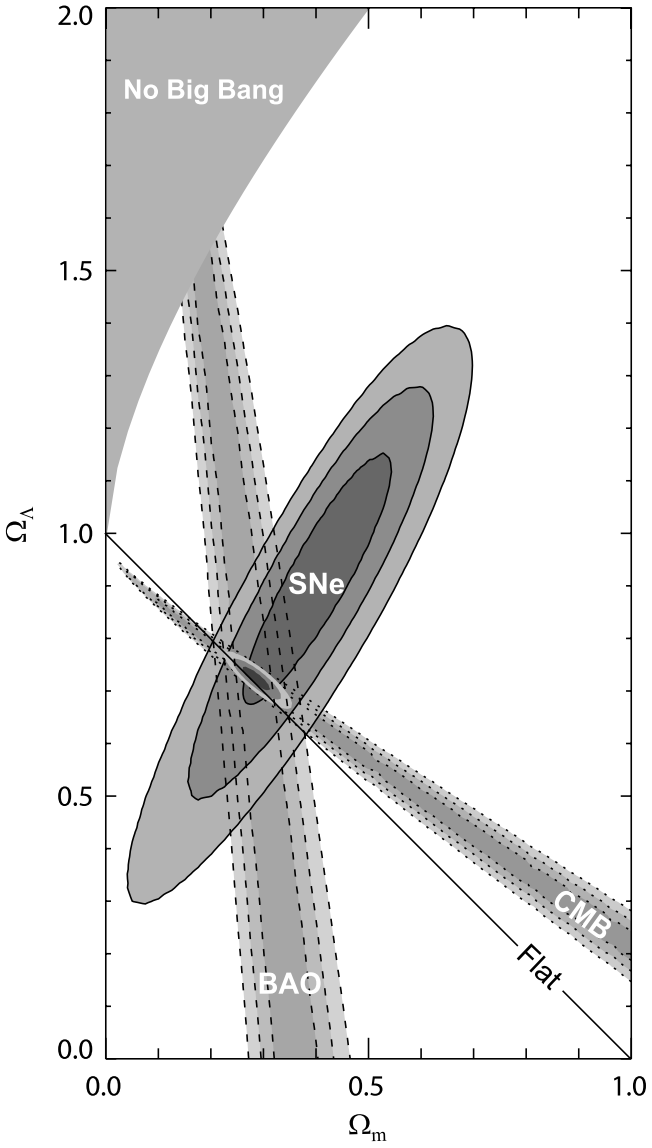

FIG. 15.—Contours at 68.3%, 95.4%, and 99.7% confidence level on Ω_Λ and Ω_M obtained from CMB, BAO, and the Union SN set, as well as their combination (assuming $w = -1$). [*See the electronic edition of the Journal for a color version of this figure.*]

Figure 16 (*left*) shows the combination of the SN data with either the CMB constraints or the BAO constraints. The results are similar; note that including either one results in a sharp cutoff at $w_0 + w_a = 0$, from the physics as mentioned in regards to equation (8). Since $w(z \gg 1) = w_0 + w_a$ in this parameterization, any model with more positive high-redshift w will not yield a matter-dominated early universe, altering the sound horizon in conflict with observations.

Note that BAO do not provide a purely "low" redshift constraint, because implicit within the BAO data analysis, and hence the constraint, is that the high-redshift universe was matter-dominated (so the sound horizon at decoupling is properly calculated). Thus, one cannot avoid the issue of modeling how the dark energy EOS behaves at high redshifts by using this constraint rather than the CMB. (We differ here from Riess et al. 2007, who treat BAO as a low-redshift constraint.) SN data are especially useful in constraining $w(z)$ because there is no dependence at all on the high-redshift behavior, unlike CMB and BAO data.

As one might expect, because of the different orientations of the confidence contours and the different physics that enters, combining both the CMB and BAO constraints with the SN data clears up the degeneracies somewhat, as seen in Figure 16, with and without systematics. Inclusion of curvature does not substantially increase the contours.

We emphasize that the wall in w_0-w_a space is not imposed a priori and does not represent a breakdown of the parameterization, but a real physical effect from violating early matter domination. Nevertheless, we can ask what limits could be put on the early dark energy behavior—either its presence or its equation of state—if we do not use the w_0-w_a parameterization. A simple but general model for $w(z)$ creates a series of redshift bins and assumes w is constant over each bin. The constraints from this are shown in Figure 17. Note that the data points are correlated.

Riess et al. (2007) made a somewhat similar investigation with the emphasis on the impact of the highest-redshift SNe. A difference to the work of Riess et al. (2007) is that we do not decorrelate the constraints in the different redshift bins. While this implies that the binwise constraints shown in Figure 17 are correlated, it ensures that the w-constraints shown for a given bin are confined to the exact redshift range of the bin. If instead one applies a decorrelation procedure, some of the tight constraints from lower redshifts feed through to higher redshifts (i.e., $z > 1$). See de Putter & Linder (2007) for general discussion of this issue. Unlike Riess et al. (2007) we additionally place a w bin at higher redshift than the SN data ($z > 2$), to account for the expansion history of the early universe, and do not fix w in this bin. The Riess "strong" prior has a fourth bin for $z > 1.8$, but fixes $w = -1$. The "strongest" prior does not have a fourth bin. Forcing either of these behaviors on the $z > 2$ universe results in unfairly tight constraints and the danger of bias (Linder 2007; de Putter & Linder 2007); in failing to separate the SN bins from those of the CMB and BAO essentially the entire constraint in the redshift $z \gtrsim 1$ bin is from the CMB (see also Wright 2007).

Consider the top row of Figure 17. These results are for bins with $z < 0.5$, $0.5 < z < 1.0$, $1.0 < z < 2.0$, and $z > 2.0$. The only constraint that can be concluded from the highest-redshift bin is that $w_{[2,\infty]} \lesssim 0$, but this constraint comes entirely from CMB and BAO, which requires that the early universe is matter-dominated (see the above discussion of the wall in the w_a-w_0 plane). We then look at the $z = 1$–2 bin for constraints on w, which would be due to the $z > 1$ SNe and we find essentially no constraint.

The lowest-redshift bin is constrained to $w_{[0,0.5]} \approx -1 \pm 0.1$. The next bin is compatible with -1, but the central value is high. This deviation from -1 seems to be due to the unexpected brightness (by about 0.1 mag) of the Hubble data at $z > 1$ (see Fig. 10). (Recall that w at some z influences distances at larger redshifts.) We clearly see that to be sensitive to appreciable deviations from $w = -1$ such as 0.1 mag at $z \sim 1$, which is key to constraining theories of dark energy, one requires better statistics for the very high-redshift supernovae (and comparably good systematics).

Given that the strongest constraints on w are contained in the first bin, one might attempt to search for a redshift dependence of w at lower redshifts by changing the borders of the bins. The smallest errors are obtained roughly with the binning $z < 0.1$,

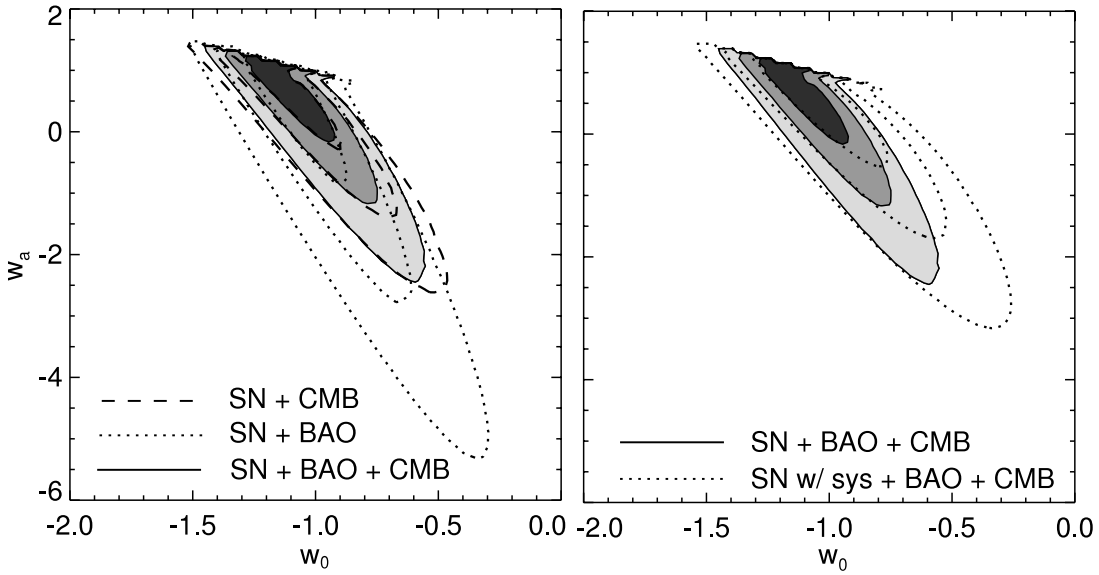

FIG. 16.—Contours at 68.3%, 95.4%, and 99.7% confidence level on w_a and w_0 for a flat universe. *Left*: The Union SN set was combined with CMB or BAO constraints. *Right*: Combination of SNe, CMB, and BAO data, with and without systematic uncertainties included. The diagonal line represents $w_0 + w_a = 0$; note how the likelihoods based on observational data remain below it, favoring matter domination at $z \gg 1$. [*See the electronic edition of the Journal for a color version of this figure.*]

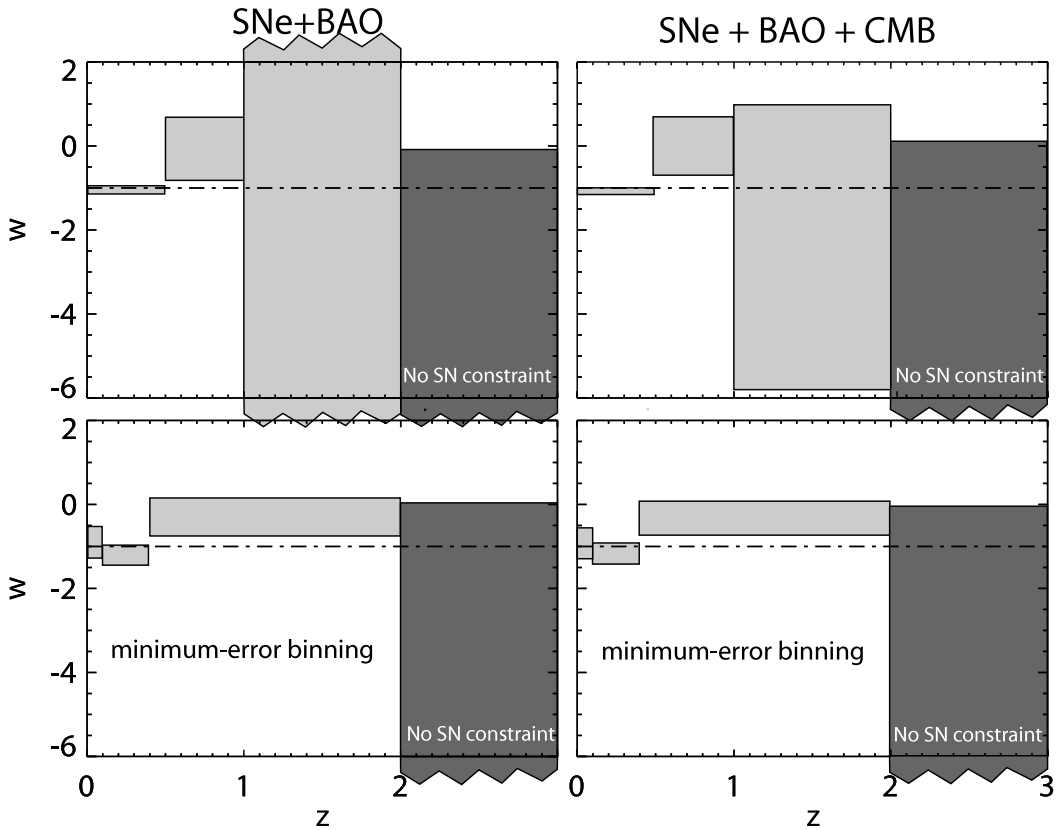

FIG. 17.—Constraints at 68% confidence level on $w(z)$, where $w(z)$ is assumed to be constant over each redshift bin. The left column combines the Union SN set with BAO constraints only, while the right column includes also constraints from the CMB. The top row illustrates the fact that only extremely weak constraints on the equation of state exist at $z > 1$. The bottom row shows a different binning that minimizes the mean bin error. Note that for $z > 2$ (*dark gray*: No SN constraint) only upper limits exist, basically enforcing matter domination, coming from either CMB data or, in the case without CMB data, from requiring substantial structure formation (a linear growth factor within a factor of 10 of that observed).

$0.1 < z < 0.4$, $0.4 < z < 2.0$, and $2.0 < z$. These constraints are shown in the bottom row of Figure 17. The results are similar to the results from the other binning, with the lowest two bins centered around $w = -1$ and the next bin centered around a more positive value. No significant redshift dependence is observed. Note the tight limit on the $0.4 < z < 2$ bin is *not* saying $w(z > 1) \approx -1$, even approximately, since the leverage on $w(z)$ is coming from the $0.4 < z < 1$ part of the bin (this illustrates the importance of considering multiple binnings).

To sum up, even in combination with current BAO and CMB data, current SN data sets cannot tell us whether an energy density component other than matter existed at $z > 1$ and cannot tell us whether such a component, if it existed, had an equation of state with negative pressure. In the future, however, SN data that achieve Hubble diagram accuracy of 0.02 mag out to $z = 1.7$ will be able to address these questions and provide independent checks of the $z > 1$ universe.

Note that while constraints on a possible redshift dependency of w have been shown in Figures 16 and 17, we do not present values for the projected, one-dimensional constraints for several reasons. First, the bounds are still very weak and as a result the error bars show highly non-Gaussian errors (as visible in Fig. 16). In addition, our treatment of systematic errors has not been optimized for a redshift-dependent w and a potential systematic redshift dependence of the distance modulus is only partially taken into account. As a consequence, the resulting (already large) systematic errors on $w(z)$ would be underestimated.

In this analysis so far we have not excluded any SNe based on extreme values of stretch or color, therefore including also the peculiar class of underluminous 1991bg-like SNe that are typically associated with small stretch values. After unblinding, in an effort to study the robustness of our results, we have introduced a stretch cut, $s > 0.6$, to eliminate SN1991bg-like SNe from the sample. The most significant consequence of this cut came with the removal of SN 1995ap, a supernova in the Riess et al. (1998) sample. By itself the removal of this one supernova can change the cosmological fitted parameters in the Ω_M-Ω_Λ and Ω_M-w planes by nearly 1 σ along the more degenerate contour axis (and away from a flat universe). However, without SN 1995ap, the test for tension between data sets that we applied in § 4.4 would show the Riess et al. (1998) data set to be a 3.5 σ outlier and one would be forced, unless the tension can be resolved otherwise, to remove the data set from the compilation. The net result of the $s > 0.6$ cut would then be a 0.25 σ change in w, Ω_M, and Ω_Λ in the direction of the more degenerate contour axis. The results presented in this paper are based on the sample without the stretch cut; however, since the parameters along the direction of the degeneracy are well constrained once CMB or BAO data are added, the combined constraints essentially do not depend on whether or not the stretch cut is applied.

7. CONCLUSION

The cosmological parameter constraints from the Union SN Ia compilation shown in Figures 12, 14, 16, and 17 reflect the current best knowledge of the world's Type Ia supernova data sets. Specifically, in addition to the older data, they include the new data sets of nearby Hubble-flow SNe Ia we presented in this paper, the recent large, homogeneous, high–S/N SNLS and ESSENCE data sets published by Astier et al. (2006) and Miknaitis et al. (2007) as well as the high-redshift supernovae in Riess et al. (2004, 2007). Equally important is that a number of outstanding analysis issues have been addressed that improve the reliability and reduce the biases of the current Union SN Ia compilation, and should stand us in good stead for future compilations. We are making the ingredients and results of the Union compilation available at the associated Web site (see footnote 42), and we intend to provide occasional updates to this as new information becomes available.

Several conclusions can be drawn from the new larger SCP Union SN Ia compilation that could not be approached with smaller data sets. In particular, the large statistics can be used to address systematic uncertainties in novel ways.

We test for evolution by subdividing the sample into low-stretch and high-stretch SNe. According to recent evidence (Sullivan et al. 2006) these two samples might be dominated by different progenitor systems (Scannapieco & Bildsten 2005; Mannucci et al. 2006), which are likely to show different evolutions. Hence, performing consistent but independent cosmology fits for the two subsamples provides a powerful test for potential evolutionary effects. The resulting cosmological fitted parameters are found to be consistent. This comparison is particularly meaningful, as the statistical uncertainties from the subsamples are comparable to the total (stat+sys) uncertainties obtained from the full sample.

With the larger Union data set, it is possible to begin to examine the rate of true outliers from the Hubble-plot fit. It appears that the current selection criteria for SNe Ia can find very homogeneous sets of supernovae, but not perfectly homogeneous sets. With these criteria, there are apparently true outliers, at the percent level for the SNLS sample and up to 10% for other samples. The analysis performed here was made robust to outliers, reducing the associated error on cosmological parameters to a level comparable to other sources of systematic error.

Compilations offer the chance to test for observer-dependent systematic effects, i.e., tension between the data sets. The blind analysis performed here is an important element in rigorous estimation of systematics. While in general we find a high degree of consistency between samples, we see modest tension when comparing the slope of the Hubble residuals as a function of redshift, $d\mu/dz$. For the present compilation, our cosmology results are expected to hold within the quoted systematic uncertainties. However, once the homogeneous data sets get larger—and the systematic errors dominate over the statistical ones for the different sets—such tests will become even more important, as they allow one to perform cross-checks with different data sets calibrated in different ways. Future data samples can be added to the Union set, by first blinding the data and then performing a diagnostic analysis similar to the one performed here. Only after any inconsistencies can be resolved, would the new data be unblinded.

We proposed a scheme to incorporate both sample-dependent and common systematic errors. We showed in § 5 that systematic errors can be approached by treating the systematics as a normal distribution of a parameterized systematic term. We find that the combination of SNe constraints with CMB constraints, due to their larger complementarity with SNe data, results in smaller systematic errors than the combination with BAO constraints. Adding BAO, CMB, and SNe constraints leads to yet smaller statistical error bars, while the error bars including systematics do not improve.

The robustness of the detection of the accelerating expansion of the universe is continually increasing as improved systematics analysis is reinforced by larger SN data sets. The current

knowledge of the nature of dark energy is still modest, however, with the uncertainty on the assumed-constant equation of state only under 10% *if* multiple probes are combined. The current "world" estimate presented here employing the full set of current SN data, plus other measurements, gives a best constraint of $w = -0.969^{+0.059}_{-0.063}(\mathrm{stat})^{+0.063}_{-0.066}(\mathrm{sys})$ on a constant EOS parameter w at 68.3% confidence level. However, allowing for time variation in the dark energy equation of state further opens the possibilities for the physics driving the acceleration, consistent with all current observations. In particular, present SN data sets do not have the sensitivity to answer the questions of whether dark energy persists to $z > 1$ or whether it had negative pressure then.

On the positive side, with the more sophisticated analyses and tests carried out here, we still have encountered no limits to the potential use of future, high-accuracy SN data as cosmological probes. New data sets for nearby, moderate-redshift, and high-redshift well-characterized SNe Ia are forthcoming and we expect realistic, robust constraints to catch up with our optimistic hopes on understanding the accelerating universe.

This work is based on observations made with: the Lick and Keck Observatories; the Cerro Tololo Inter-American Observatory 4 m Blanco Telescope; the Yale/AURA/Lisbon/OSU (YALO) 1 m Telescope at Cerro Tololo Inter-American Observatory; the Apache Point Observatory 3.5 m telescope, which is owned and operated by the Astrophysical Research Consortium; the WIYN Observatory, owned and operated by the WIYN Consortium, which consists of the University of Wisconsin, Indiana University, Yale University, and the National Optical Astronomy Observatory (NOAO); the Isaac Newton Telescope, which is operated on the island of La Palma by the Isaac Newton Group in the Spanish Observatorio del Roque de los Muchachos of the Instituto de Astrofísica Canarias; the Nordic Optical Telescope, operated on the island of La Palma jointly by Denmark, Finland, Iceland, Norway, and Sweden, in the Spanish Observatorio del Roque de los Muchachos of the Instituto de Astrofisica de Canarias; and the MDM Observatory 2.4 m Hiltner Telescope. The authors wish to thank the telescope allocation committees and the observatory staffs for their support for the extensive supernova search campaign and follow-up observations that contributed to the results reported here. In particular, we wish to thank C. Bailyn and S. Tourtellotte for assistance with YALO observations, D. Harner for obtaining WIYN data, and D. Folha and S. Smartt for the INT 2.5 m service observing. For their efforts in the coordinated supernova search, we wish to acknowledge the NEAT search team (E. Helin, S. Pravdo, D. Rabinowitz, and K. Lawrence) at JPL and the Spacewatch program at the University of Arizona (which includes R. S. McMillan, T. Gehrels, J.A. Larsen, J. L. Montani, J. V. Scotti, N. Danzl, and A. Gleason). We also wish to thank B. Schmidt, A. Filippenko, M. Schwartz, A. Gal-Yam, and D. Maoz for providing us with early announcements of supernova candidates.

This work was supported in part by the Director, Office of Science, Office of High Energy and Nuclear Physics, US Department of Energy, through contract DE-AC02-05CH11231. This research used resources of the National Energy Research Scientific Computing Center, which is supported by the Office of Science of the US Department of Energy under contract DE-AC02-05CH11231. The use of Portuguese time for the YALO telescope was supported by Fundação para a Ciência e Tecnologia, Portugal, and by Project PESO/ESO/P/PRO/1257/98.

M. K. acknowledges support from the Deutsche Forschungsgemeinschaft (DFG). P. E. N. acknowledges support from the US Department of Energy Scientific Discovery through Advanced Computing program under contract DE-FG02-06ER06-04. A. M. M. acknowledges financial support from Fundação para a Ciência e Tecnologia (FCT), Portugal, through project PESO/P/PRO/15139/99.

APPENDIX A

INSTRUMENTS AND COLOR TERMS

The color terms obtained for all instruments are summarized in Table 7. Table 8 shows the applied shifts of the passbands, which are needed to reproduce the colors of the observed standard and field stars.

TABLE 7
Color Terms for Instruments and Bands

Telescope and Instrument	c_b^{bv}	c_v^{bv}	c_r^{vr}	c_i^{vi}
CTIO 1.5 m SITE2K6	−0.095 (0.003)	0.029 (0.001)	0.028 (0.002)	0.018 (0.001)
CTIO 1.5 m TK1	−0.017 (0.002)	0.037 (0.001)	0.026 (0.002)	0.015 (0.001)
CTIO 0.9 m TK2	−0.097 (0.005)	0.016 (0.002)	0.006 (0.004)	0.022 (0.002)
DANISH DFOSC	0.133 (0.002)	0.033 (0.001)	0.067 (0.001)	−0.000 (0.3001)
JKT Tek1	0.055 (0.006)	0.020 (0.004)	0.030 (0.008)	0.053 (0.007)
LICK 1 m DEWAR2	0.094 (0.007)	−0.026 (0.007)	−0.052 (0.007)	0.018 (0.004)
LICK 1 m DEWAR5	0.226 (0.033)	−0.073 (0.016)	−0.106 (0.007)	0.034 (0.002)
YALO ANDICAM	0.094 (0.002)	−0.035 (0.001)	0.373 (0.002)	−0.041 (0.001)
ESO 3.6 m EFOSC	0.048 (0.005)	0.048 (0.002)	0.048 (0.002)	−0.010 (0.001)
KPNO 2.1 m T1KA	0.103 (0.006)	−0.021 (0.002)	0.029 (0.007)	0.023 (0.002)
CFHT STIS2	0.105 (0.009)	0.002 (0.009)	−0.079 (0.005)	0.043 (0.002)
WIYN S2KB	0.059 (0.019)	−0.002 (0.019)	−0.018 (0.035)	0.016 (0.015)
MARLY	...	...	−0.296 (0.003)	−0.017 (0.002)

TABLE 8
THE APPLIED SHIFTS OF THE PASSBANDS, WHICH ARE NEEDED TO REPRODUCE THE COLORS OF THE OBSERVED STANDARD AND FIELD STARS

Instrument	$\Delta\lambda_B$ (Å)	$\Delta\lambda_V$ (Å)	$\Delta\lambda_R$ (Å)	$\Delta\lambda_I$ (Å)
CTIO 1.5 m SITE2K6	−20	0	−30	80
CTIO 1.5 m SITE2K6 (small)	−20	0	−30	90
CTIO 1.5 m TK1	10	−10	−40	90
CTIO 0.9 m TK2	−10	−10	−10	−10
DANISH DFOSC	100	30	30	50
JKT Tek1	0	−20	−50	60
LICK 1 m DEWAR5 (small)	90	−10	−30	−40
LICK 1 m DEWAR2	90	10	−10	0
LICK 1 m DEWAR5	100	−30	−40	0
YALO ANDICAM	10	−20	−340	−50
ESO 3.6 m EFOSC	20	−20	0	50
KPNO 2.1 m T1KA	−30	−30	−40	−60
CFHT STIS2	−70	−10	−100	−50

APPENDIX B

TERTIARY STANDARD STAR CATALOG

Table 9 lists the coordinates and magnitudes of the tertiary calibration stars.

TABLE 9
COORDINATES AND MAGNITUDES OF TERTIARY CALIBRATION STARS

Number	R.A. (J2000.0)	Decl. (J2000.0)	V	$B-V$	$V-R$	$V-I$
			SN 1999aa			
1	08 27 37.43	21 31 18.8	14.495 (0.003)	0.5145 (0.006)	0.3005 (0.005)	0.6109 (0.006)
2	08 27 41.27	21 25 01.9	14.978 (0.006)	0.6927 (0.013)	0.4188 (0.004)	0.2622 (0.008)
3	08 28 02.64	21 33 56.1	14.817 (0.005)	0.9347 (0.014)	0.4969 (0.004)	0.1772 (0.012)
4	08 27 38.16	21 29 54.5	15.115 (0.004)	0.6558 (0.008)	0.4143 (0.004)	0.7879 (0.006)
5	08 27 47.99	21 33 01.1	15.550 (0.007)	0.5243 (0.010)	0.3240 (0.005)	0.6872 (0.007)
6	08 27 44.64	21 31 11.6	15.382 (0.004)	0.7130 (0.010)	0.4010 (0.004)	0.7809 (0.007)
7	08 27 48.47	21 33 20.1	15.575 (0.008)	0.5614 (0.016)	0.3434 (0.006)	0.7287 (0.008)
8	08 27 21.11	21 29 17.8	15.438 (0.007)	0.7989 (0.015)	0.4610 (0.005)	0.8839 (0.007)
9	08 27 55.51	21 24 46.4	15.693 (0.008)	0.6203 (0.018)	0.3835 (0.006)	0.8045 (0.008)
10	08 27 29.04	21 27 07.9	15.514 (0.006)	0.8045 (0.013)	0.4345 (0.005)	0.6378 (0.008)

NOTE.—Units of right ascension are hours, minutes, and seconds, and units of declination are degrees, arcminutes, and arcseconds. Uncertainties are given in parentheses. Table 9 is available in its entirety in the electronic edition of the *Astrophysical Journal*. A portion is shown here for guidance regarding its form and content.

APPENDIX C

LIGHT CURVES FROM THE NEARBY SUPERNOVA CAMPAIGN

Table 10 shows the *BVRI* magnitudes from the Nearby Supernova Campaign. The fitted light curve parameters of all SNe can be found in Table 11.

TABLE 10
BVRI Magnitudes

JD	Telescope	*B*	*V*	*R*	*I*
		SN 1999aa			
221.81.....	LICK 1 m DEWAR2	15.828 (0.032)	...	...	...
222.67.....	YALO	15.642 (0.018)	15.680 (0.028)	15.689 (0.040)	15.717 (0.105)
223.67.....	YALO	15.462 (0.020)	...	15.486 (0.036)	15.514 (0.083)
225.65.....	YALO	15.211 (0.017)	15.260 (0.028)	15.276 (0.030)	15.312 (0.025)
227.73.....	LICK 1 m DEWAR2	15.006 (0.016)	15.060 (0.024)	15.080 (0.018)	...
229.62.....	YALO	14.924 (0.017)	14.965 (0.026)	15.092 (0.030)	...
232.61.....	YALO	14.908 (0.017)	14.913 (0.028)	15.062 (0.030)	15.253 (0.025)
235.60.....	YALO	14.919 (0.021)	14.898 (0.032)	15.037 (0.031)	15.307 (0.029)
241.60.....	YALO	15.183 (0.013)	15.062 (0.027)	15.266 (0.030)	15.575 (0.024)
243.88.....	LICK 1 m DEWAR5	...	...	15.236 (0.051)	15.724 (0.039)

Notes.—Uncertainties are given in parentheses. Table 10 is available in its entirety in the electronic edition of the *Astrophysical Journal*. A portion is shown here for guidance regarding its form and content.

TABLE 11
Supernovae of the Union Compilation

Name	*z*	$m_B^{\max}$	*s*	*c*	μ	Reference	Cut
1993ag.....	0.0500	17.79 (0.05)	0.91 (0.02)	0.09 (0.02)	36.77 (0.15)	1	
1993o.....	0.0529	17.61 (0.05)	0.90 (0.01)	−0.01 (0.02)	36.82 (0.15)	1	
1993h.....	0.0251	16.74 (0.09)	0.68 (0.01)	0.21 (0.01)	35.17 (0.17)	1	
1993b.....	0.0701	18.38 (0.09)	0.99 (0.03)	0.04 (0.04)	37.57 (0.15)	1	
1992bs.....	0.0627	18.18 (0.05)	1.00 (0.02)	−0.03 (0.02)	37.55 (0.15)	1	
1992br	0.0876	19.40 (0.11)	0.65 (0.04)	0.03 (0.05)	38.19 (0.16)	1	
1992bp.....	0.0786	18.28 (0.03)	0.87 (0.02)	−0.04 (0.02)	37.52 (0.15)	1	
1992bo.....	0.0172	15.75 (0.13)	0.74 (0.01)	0.03 (0.01)	34.65 (0.19)	1	
1992bl	0.0422	17.29 (0.06)	0.79 (0.02)	−0.01 (0.02)	36.36 (0.15)	1	
1992bh.....	0.0453	17.59 (0.05)	0.98 (0.01)	0.10 (0.01)	36.66 (0.15)	1	

Notes.—Uncertainties are given in parentheses. Explanation of cuts: (o) 3 σ outlier; (p) insufficient early data; (c) no color; (d) too few data points; (f) fit not converged. Table 11 is available in its entirety in the electronic edition of the *Astrophysical Journal*. A portion is shown here for guidance regarding its form and content.

References.—(1) Hamuy et al. 1996; (2) Krisciunas et al. 2004a, 2004b; (3) Riess et al. 1999; (4) Jha et al. 2006; (5) this work; (6) Riess et al. 1998 + HZT; (7) Perlmutter et al. 1999; (8) Tonry et al. 2003; (9) Barris et al. 2004; (10) Knop et al. 2003; (11) Riess et al. 2007; (12) Astier et al. 2006; (13) Miknaitis et al. 2007.

APPENDIX D

LIGHT CURVE DATA FROM PERLMUTTER ET AL.

The photometric light curve data from the 42 supernovae of Perlmutter et al. (1999) are shown in Table 12.

TABLE 12
THE PHOTOMETRIC LIGHT CURVE DATA FROM THE 42 SUPERNOVAE OF PERLMUTTER ET AL. (1999)

R			*I*		
MJD	Flux ($zp = 30$ mag)	σ(flux)	MJD	Flux ($zp = 30$ mag)	σ(flux)
SN 1997s ($z = 0.612$)					
50431.85.....	9.89E+01	5.71E+01	50459.04	5.84E+02	2.20E+02
50432.82.....	1.11E+02	5.85E+01	50465.96	3.68E+02	3.64E+02
50454.82.....	6.49E+02	4.05E+01	50466.92	7.34E+02	2.29E+02
50459.01.....	5.49E+02	4.47E+01	50480.86	4.28E+02	9.23E+01
50462.82.....	6.82E+02	4.05E+01	50489.79	9.54E+02	1.16E+02
50465.82.....	5.92E+02	7.19E+01	50513.78	4.54E+02	1.85E+02
50480.83.....	2.18E+02	3.04E+01	50514.77	6.36E+02	1.06E+02
50489.76.....	2.37E+02	3.30E+01	50518.77	3.95E+02	1.51E+02
50513.74.....	4.10E+01	2.98E+01			
50514.73.....	6.83E+01	6.09E+01			

NOTES.—Data consist of Bessell *R* and *I* band data and are presented as flux, with a common zero point of $zp = 30$ mag. Multiple data points for a given night were combined into a single data point. Since reference images were used to subtract the host galaxy light, the data points are correlated. We recommend using the data from http://supernova.lbl.gov/Union, which includes the covariance matrix. More information about the SNe can be found in Perlmutter et al. (1999). Table 12 is available in its entirety in the electronic edition of the *Astrophysical Journal*. A portion is shown here for guidance regarding its form and content.

REFERENCES

Aguirre, A. 1999, ApJ, 525, 583
Aldering, G. 2000, in AIP Conf. Ser. 522, Cosmic Explosions: Tenth Astrophysics Conference, ed. S. S. Holt & W. W. Zhang (New York: AIP), 75
———. 2005, NewA Rev., 49, 346
Aldering, G., Nugent, P., Helin, E., Pravdo, S., Rabinowitz, D., Lawrence, K., Kunkel, W., & Phillips, M. 1999, IAU Circ., 7122, 1
Altavilla, G., et al. 2004, MNRAS, 349, 1344
Armstrong, M., & Schwartz, M. 1999, IAU Circ., 7108, 1
Astier, P., et al. 2006, A&A, 447, 31
Barris, B. J., et al. 2004, ApJ, 602, 571
Bergström, L., Goliath, M., Goobar, A., & Mörtsell, E. 2000, A&A, 358, 13
Bessell, M. S. 1990, PASP, 102, 1181
Blanc, G., et al. 2004, A&A, 423, 881
Bohlin, R. C., & Gilliland, R. L. 2004, AJ, 127, 3508
Cardelli, J. A., Clayton, G. C., & Mathis, J. S. 1989, ApJ, 345, 245
Conley, A., Carlberg, R. G., Guy, J., Howell, D. A., Jha, S., Riess, A. G., & Sullivan, M. 2007, ApJ, 664, L13
Conley, A., et al. 2006, ApJ, 644, 1
Davis, T. M., et al. 2007, ApJ, 666, 716
de Putter, R., & Linder, E. V. 2007, preprint (arXiv:0710.0373)
Dunkley, J., et al. 2008, preprint (arXiv:0803.0586)
Eisenstein, D. J., et al. 2005, ApJ, 633, 560
Filippenko, A. V., Li, W. D., Treffers, R. R., & Modjaz, M. 2001, in ASP Conf. Ser. 246, IAU Colloq. 183, Small Telescope Astronomy on Global Scales, ed. B. Paczynski, W.-P. Chen, & C. Lemme (San Francisco: ASP), 121
Folatelli, G. 2004, Ph.D. thesis, Stockholm Univ.
Gal-Yam, A., Maoz, D., Guhathakurta, P., & Filippenko, A. 2008, ApJ, 680, 550
Gal-Yam, A., et al. 1999, IAU Circ., 7130, 1
Garavini, G., et al. 2004, AJ, 128, 387
———. 2005, AJ, 130, 2278
———. 2007, A&A, 470, 411
Garnavich, P. M., et al. 1998, ApJ, 493, L53
Germany, L. M., Reiss, D. J., Schmidt, B. P., Stubbs, C. W., & Suntzeff, N. B. 2004, A&A, 415, 863
Goldhaber, G., et al. 2001, ApJ, 558, 359
Gott, J. R. I., Vogeley, M. S., Podariu, S., & Ratra, B. 2001, ApJ, 549, 1
Gunn, J. E., & Stryker, L. L. 1983, ApJS, 52, 121
Guy, J., Astier, P., Nobili, S., Regnault, N., & Pain, R. 2005, A&A, 443, 781
Guy, J., et al. 2007, A&A, 466, 11
Hamuy, M., et al. 1996, AJ, 112, 2408
Holz, D. E., & Linder, E. V. 2005, ApJ, 631, 678
Howell, D. A., Sullivan, M., Conley, A., & Carlberg, R. 2007, ApJ, 667, L37
Jha, S., Riess, A. G., & Kirshner, R. P. 2007, ApJ, 659, 122
Jha, S., et al. 2006, AJ, 131, 527
Jönsson, J., Dahlén, T., Goobar, A., Gunnarsson, C., Mörtsell, E., & Lee, K. 2006, ApJ, 639, 991
Kim, A., Regnault, N., Nugent, P., Aldering, G., Dahlen, T., Goobar, A., & Hook, I. 1999a, IAU Circ., 7136, 1
Kim, A., et al. 1999b, IAU Circ., 7117, 1
Knop, R. A., et al. 2003, ApJ, 598, 102
Komatsu, E., et al. 2008, preprint (arXiv:0803.0547)
Krisciunas, K., Hastings, N. C., Loomis, K., McMillan, R., Rest, A., Riess, A. G., & Stubbs, C. 2000, ApJ, 539, 658
Krisciunas, K., et al. 2001, AJ, 122, 1616
———. 2004a, AJ, 127, 1664
———. 2004b, AJ, 128, 3034
Landolt, A. U. 1992, AJ, 104, 340
Linder, E. V. 1988, A&A, 206, 190
———. 2003, Phys. Rev. Lett., 90, 091301
———. 2006, Phys. Rev. D, 74, 103518
———. 2007, preprint (arXiv:0708.0024)
Linder, E. V., & Miquel, R. 2004, Phys. Rev. D, 70, 123516
Mannucci, F., Della Valle, M., & Panagia, N. 2006, MNRAS, 370, 773
Miknaitis, G., et al. 2007, ApJ, 666, 674
Mörtsell, E., & Goobar, A. 2003, J. Cosmol. Astropart. Phys., 9, 9
Nugent, P., Aldering, G., & Phillips, M. M. 1999a, IAU Circ., 7133, 1
Nugent, P., Kim, A., & Perlmutter, S. 2002, PASP, 114, 803
Nugent, P., et al. 1999b, IAU Circ., 7134, 1
———. 1999c, IAU Circ., 7134, 1
Östman, L., & Mörtsell, E. 2005, J. Cosmol. Astropart. Phys., 2, 5
Parodi, B. R., Saha, A., Sandage, A., & Tammann, G. A. 2000, ApJ, 540, 634
Percival, W. J., Cole, S., Eisenstein, D. J., Nichol, R. C., Peacock, J. A., Pope, A. C., & Szalay, A. S. 2007, MNRAS, 381, 1053
Perlmutter, S., & Schmidt, B. P. 2003, in Supernovae and Gamma-Ray Bursters, ed. K. Weiler (Berlin: Springer), 195

Perlmutter, S., et al. 1997, ApJ, 483, 565
———. 1998, Nature, 391, 51
———. 1999, ApJ, 517, 565
Phillips, M. M. 1993, ApJ, 413, L105
Pravdo, S. H., et al. 1999, AJ, 117, 1616
Qiao, Q. Y., Wei, J. Y., Qiu, Y. L., & Hu, J. Y. 1999, IAU Circ., 7109, 3
Rengstorf, A. W., et al. 2004, ApJ, 606, 741
Riess, A. G., et al. 1998, AJ, 116, 1009
———. 1999a, AJ, 117, 707
———. 2004, ApJ, 607, 665
———. 2007, ApJ, 659, 98
Reiss, D., Sabine, S., Germany, L., & Schmidt, B. 1999b, IAU Circ., 7124, 2
Ruiz-Lapuente, P. 2007, Classical Quantum Gravity, 24, 91
Sánchez, A. G., & Cole, S. 2008, MNRAS, 385, 830
Sasaki, M. 1987, MNRAS, 228, 653
Scannapieco, E., & Bildsten, L. 2005, ApJ, 629, L85
Schlegel, D. J., Finkbeiner, D. P., & Davis, M. 1998, ApJ, 500, 525
Schmidt, B. P., et al. 1998, ApJ, 507, 46
Stritzinger, M., Suntzeff, N. B., Hamuy, M., Challis, P., Demarco, R., Germany, L., & Soderberg, A. M. 2005, PASP, 117, 810
Stritzinger, M., et al. 2002, AJ, 124, 2100
Strolger, L.-G. 2003, Ph.D. thesis, Univ. Michigan
Strolger, L. G., Smith, R. C., Nugent, P., & Phillips, M. 1999a, IAU Circ., 7131, 1
Strolger, L. G., et al. 1999b, IAU Circ., 7125, 1
———. 2002, AJ, 124, 2905
Strovink, M. 2007, preprint (arXiv:0705.0726)
Stubbs, C. W., & Tonry, J. L. 2006, ApJ, 646, 1436
Sullivan, M., et al. 2003, MNRAS, 340, 1057
———. 2006, ApJ, 648, 868
Suntzeff, N. B. 2000, in AIP Conf. Ser. 522, Cosmic Explosions: Tenth Astrophysics Conference, ed. S. S. Holt & W. W. Zhang (New York: AIP), 65
Tonry, J. L., et al. 2003, ApJ, 594, 1
Tripp, R. 1998, A&A, 331, 815
Tripp, R., & Branch, D. 1999, ApJ, 525, 209
Wang, L., Strovink, M., Conley, A., Goldhaber, G., Kowalski, M., Perlmutter, S., & Siegrist, J. 2006, ApJ, 641, 50
Wood-Vasey, W. M., et al. 2007, ApJ, 666, 694
Wright, E. L. 2007, ApJ, 664, 633
Yao, W. M., et al. 2006, J. Phys. G, 33, 1